An analysis of satellite skin temperatures in the Beaufort Sea region in conjunction with in-situ air temperature measurements

Allegra Gordon

Advisor: Mary-Louise Timmermans
Second Reader: Ron Smith

April 30, 2014

A Senior Thesis presented to the faculty of the Department of Geology and Geophysics, Yale University, in partial fulfillment of the Bachelor's Degree.

Abstract

Arctic sea ice is an important climate indicator and moderates global temperatures because of its high albedo. With a warming climate, sea ice is melting faster than recovering; observing local changes in the Arctic is essential in order to best predict future temperatures. The Arctic has limited in-situ air temperature measurements, resulting in spatially sparse climate monitoring. This study hypothesizes that satellite-derived skin temperatures (T_s) can be used as a tool to estimate in-situ air temperatures (T_a) of the Arctic's Beaufort Sea region during the melting season, from April to October in 2013. This study is the first to use Landsat 8 satellite data for this purpose in the Arctic. The correlation between T_s and T_a varies between surface type (e.g. ice, melt ponds, water), with coefficients of determination ranging from 0.766 to 0.857. $T_s > T_a$ by 0.11˚C for ice and 1.91˚C for open water, confirming that T_s can be used as a tool to infer T_a in remote Arctic regions. The difference between T_s and T_a ($T_s - T_a$) has seasonal variability; $T_s > T_a$ in the onset of melting and freeze-up, while $T_s < T_a$ during the peak melting season. There is a correlation between T_s and albedo for the three surface types, with opposite phases in the seasonal cycle. Finally, I show how $T_s - T_a$ is relevant to heat flux and its seasonality between different surface types and the atmosphere. Major errors associated with recovering T_s from satellite images over a variety of Arctic surfaces are discussed.

Keywords: Arctic, sea ice, remote sensing, Landsat 8, skin temperature, heat flux, ice-albedo effect

1. Introduction

The Arctic is undergoing accelerated effects from climate change. The Arctic has experienced enhanced warming, suggested by an Arctic amplification, warming two-fold the rate of the entire northern hemisphere (Francis & Vavrus, 2012). Mean annual surface air temperature has increased by 2˚C over Arctic land, more than double the increase at lower latitudes (Overland et al., 2011). Arctic sea ice is melting at an accelerated rate. September 2012 marked the lowest minimum extent in human record; perennial ice extent has decreased from 5.8 million square kilometers to 2.6 million square kilometers, from 1957 to 2007, and is currently declining as quickly as -18% per decade (Perovich & Richter-Menge, 2009). The major factors in sea ice melt are caused by ice motion, heat budget, and ice-albedo feedback.

Therefore, it is important to monitor the quickly changing temperatures of the Arctic to better understand patterns and projections. Global land surface temperatures are expected to increase with global warming (Jin & Dickinson, 2002). The Arctic is equipped with land stations to measure air temperature along the coast (Figure 1a), as well as buoys collecting air temperature data over floating ice masses (Figure 1b). However, the spatial density of temperature stations is low and much of the sea ice is unaccounted for.

Remote sensing allows for measuring temperatures across larger scales. Satellites cannot measure air temperature, however, it is possible to calculate surface skin temperature from thermal infrared emissions.

Land surface temperatures are related to air temperature measurements, however, the two are not interchangeable (Jin & Dickinson, 2010). Surface skin temperatures (T_s) are related to radiation, surface insolation, albedo and surface type. T_s is determined by long-wave emissions from the surface and can be measured in-situ with infrared radiometers if surface emissivity is known, or calculated via satellites. Air temperature (T_a) measures the air temperature at a reference height, usually at 3 m. T_s tends to respond more quickly to changes in the land-surface boundary layer than T_a (Prigent et al., 2003).

General Circulation Models (GCM) use T_s to calculate longwave fluxes but tend to underestimate surface cooling (Prigent et al., 2003). GCMs vary in their treatment of surface and skin temperatures; some GCMs only use T_s, some only use Ta, and some use a combination of T_s and T_a. By better understanding T_s, GCMs may predict future temperature change and fluxes over a variety of surface types in the Arctic more accurately.

T_a is very homogenous and is the same over large areas. T_s, on the other hand, is very heterogeneous because it is tied to the property of the surface. Land stations and ocean/ice buoys record a uniform temperature over large areas, while the satellite-derived temperature calculates spotty surface-dependent skin temperatures. Because T_s is tied to surface properties, this study separates each satellite image into three surface types (water, melt ponds and ice) to better understand how each surface temperature is correlated to the uniform air temperature above it, and which surface plays a more dominant role in predicting air temperature. This study compares satellite-derived T_s to in-situ T_a for three surface types, and also compares each satellite scene's average T_s to T_a. The goal is to determine if T_s can be used as a tool to estimate T_a in remote Arctic areas, including sea ice regions of the Beaufort Sea.

No paper has yet applied the concept of T_s and T_a to an Arctic sea ice scene. This paper compares T_s and T_a of different surfaces in the Beaufort Sea region, using in-situ air temperatures from 15 nearby land stations (Figure 1a; Table I), five floating buoys along the Arctic coast of Alaska and Canada (Figures 1b and 1c; Table II) and 28 satellite scenes from Landsat 8 (Figure 2). The difference between T_s and T_a ($T_s - T_a$) is measured to investigate the possibility of using satellite-derived T_s to approximate T_a on a regional scale in the Beaufort Sea region.

2. Methods

a. Satellite Images

This project uses Landsat 8, the newest Landsat satellite that began normal operations on May 30, 2013. New Landsat technology includes an aerosol band, covering a wavelength window between 0.433μm and 0.453μm, a cirrus cloud band at 1270μm, as well as two

thermal infrared sensor bands at 1.560-1.660μm and 2.100-2.300μm. The temporal resolution is 16 days, and Landsat 8 covers 60% more scenes per day than Landsat 7.

Landsat is preferable over MODIS and AVHRR, two common satellites used to study the Arctic, because of its higher resolution. Landsat 8 has a resolution of 30 m for bands 1-7 and 9-11, and 15 m for band 8, the panchromatic band, whereas MODIS has a resolution of 200 m. Landsat 7 started collecting images of the Canadian Arctic, north of 80˚; however, the new Landsat 8 now captures images of the Beaufort Sea, and off-coast regions. Cells in reflective and thermal grids are 30 m by 30 m. The selected images have less than 10% cloud coverage, however, the images are further processed and masked to remove both cirrus and lower-latitude clouds. All images have been resampled and calibrated by USGS using cubic convolution into a UTM map projection with WGS84 datum. These satellite images are free and easily accessible from USGS (www.earthexplorer.usgs.gov).

Twenty-eight images of the Beaufort and Chukchi Seas from April to October are used in this study (Figures 2 and 3). Images ranged from sea ice floating in the middle of the Beaufort Gyre (Figure 4a), to sea ice near the coastline (Figure 5a), to landfast ice breaking away from the coast (Figure 6a). All images are taken within 21:00 and 23:00 UTC. The region parameters are 69˚N to 81˚N, and 126˚W to 172˚W.

b. Masking

The Arctic tends to be very cloudy, especially during dark months in winter. Even though this study occurs during well-lit months, from April to October, clouds still cover sea ice scenes. Satellites cannot penetrate clouds to measure brightness levels for albedo calculations; longwave infrared emissions are affected by clouds when measuring T_s, too. By utilizing both a 432-RGB image (clouds appear red, while ice appears blue) and Landsat 8's cirrus cloud band, clouds can be masked out. Thus, this study only measures the albedo and skin temperature of cloud-free satellite images (Figures 4c-d, 5c-e, and 6c-d). To read more details about how to mask clouds, refer to the Appendix.

c. Land cover Unsupervised Classification

Each satellite scene was separated by surface type using K-means unsupervised classification, a statistical tool that uses the minimum Euclidean distance principle to assign pixels to the nearest class centroid (Gordon, 2013; Tou & Gonzalez, 1974). Four classes were determined statistically through spectral signatures, labeled as ice, water, and two mixed pixel classes with different ratios of ice and water. One mixed pixel had a higher fraction of water than ice, representing chunks of ice smaller than 30 m floating in open water; the other mixed pixel had a higher fraction of ice than water, representing ice with water on top of it, or a melt pond (Figures 4b, 5b and 6b). Only the second mixed pixel class (melt ponds) were considered in this analysis. Images with land were separated into five classes to include the land as its own surface type, however, the land was not taken into account when measuring T_s and albedo, even if it had snow on it. The only land temperatures measured were in places where a land-surface air temperature station was located, such as Barrow, Point Hope, and Sachs Harbour, to compare T_s and in-situ T_a at the exact coordinates. Otherwise, temperatures and albedos from land regions were omitted to ensure only sea ice and seawater were evaluated (Figures 5a-e). For further details about K-means unsupervised classification, see Appendix.

d. Computing the surface albedo

Albedo measures a surface's reflectivity and is important in determining the Earth's surface heat budget. Albedo varies depending on surface type, ranging from 0 to 1. Water has a low albedo of 0.06, and thus absorbs incoming radiation. Sea ice has an albedo of 0.5-0.7; because of the Beaufort Sea's vast sea ice coverage, much of the incoming solar radiation is reflected back to space. As ice melts, albedo lowers and more energy is absorbed, resulting in increased surface temperatures. Albedo was computed for each classification, using an algorithm that weighs incoming wavelengths differently (Figures 4d, 5e, 6d; see [Gordon, 2013]). For more details, please refer to Appendix.

e. Computing T_s

To calculate T_s, the Planck function is inverted as follows:

$$T = \frac{K_2}{\ln\left(\frac{K_1 * \varepsilon}{CV_{R1}} + 1\right)}$$

where T is degrees in Kelvin, K1 and K2 are given by Landsat 8 thermal band metadata, CV_{R1} is the given cell value in radiance, and ε is the emissivity (Figures 4c, 5c-d and 6c). This study uses 0.95 as an approximation for a typical emissivity (Gordon, 2013). For full details, please refer to Appendix.

f. Sources of Error in T_s values

Throughout the report, anomalously low (water) and high (ice) T_s are reported. That is, in some cases, a water class has below-freezing temperatures (colder than about -2˚C for seawater), and an ice class has above freezing temperatures (warmer than about 0˚C). A brief discussion of sources of errors is given before the main results are presented so that the reader is aware of the limitations of the present technique. Anomalous T_s values can likely be attributed primarily to errors in classifications. Surrounding ice chunks contaminate water pixels, making an apparent "water" class seem colder than it should be; similarly, the "ice" class can be contaminated by relatively warm water.

Thermal infrared radiation (TIR) is used to determine skin temperatures. The longer wavelengths are less energetic, requiring a lower spatial resolution. Thus, when using the TIR band, pixel size increases from 30 m to 100 m. T_s, therefore, is averaged for the 100 m-pixel before it is interpolated and calibrated into nine 30 m pixels. For a boundary region where ice and water touch, if 75% of the 100 m-pixel region is water and 25% is ice, then it is classified as "water". However, the temperature of this water class will be influenced by the presence of ice and will show a lower temperature than a 100m pixel that is 100% water. When the 100 m pixel is interpolated and calibrated, the nine 30 m pixels will share the same temperature. Thus, surface type classification is not perfect in regions containing a non-negligible fraction of both types. T_s of water is anomalously low in April, when sea ice covers a majority of the image and water is only present as leads (i.e. cracks or openings) in the sea ice pack. T_s of ice is anomalously high during the peak of the melting season in June, July and August, when smaller sea ice floes are surrounded by vast open water. Low spatial resolution of the TIR band creates more variability in temperatures at boundary regions between sea ice and water.

Note that when the classes are appropriately broken down and only the open water class is accounted for, temperatures fall within the expected range, clustering around -2˚C in April. Similarly, ice can be further separated into two sub-classes of pure ice and melting ice, which are associated with different T_s and albedos. When only pure ice is taken into consideration in the "ice" class, T_s is lower and closer to 0˚C in the dead of summer, as expected.

Clouds are a common source of error in remote sensing. T_s is influenced by cloud-top temperature, causing a reduction in expected T_s. For example, comparison of temperatures computed in the presence and absence of clouds for two images in September 2013 (image 24 and 25, [see Figure 3]) indicated that clouds lowered T_s by about 0.2˚C for all classes. Studies shows that the temperature reduction in the presence of clouds is even greater, at 0.8˚C (Casey & Cornillon, 1998). In this study, all visible clouds are masked out, reducing the potential for errors. Landsat 8 has a separate band that captures cirrus clouds, however, some images have poor resolution, making cirrus clouds indistinguishable. Thus, T_s may appear lower than expected due to cirrus cloud errors, perhaps responsible in part for anomalously low water temperatures.

During this study, USGS recalibrated all Landsat 8 images because the TIR bands were producing temperatures up to 2.1˚C inaccurate (USGS, 2014). However, this study separately tested four recalibrated images and found discrepancies in skin temperature of no more than 0.5˚C between the calibrated and uncalibrated images.

Although the skin temperature values may be more than several degrees too warm or cold for a given class in some cases, the general trends and relationships described in this study are appropriate, and patterns and seasonal variation are as would be expected from the governing physics. Future study of Landsat 8 processing and analysis techniques to improve the classification and reduce skin temperature errors is warranted. It would be further useful to compare accuracy in Arctic regions to the mid-latitudes where surface types differ.

g. Selecting In-Situ T_a Measurements

Fifteen land meteorological stations were selected from the Alaska and Canada Arctic coastline for in-situ T_a measurements (Figure 1a; Table I). Historical climate data are downloadable from Weather Underground (www.wunderground.com) and USGS (www.pubs.usgs.gov). All land station T_a data are taken within the same hour as T_s data derived from satellite measurements. T_a is measured 3 m above ground; however, the elevations of the stations vary from 2 to 95 m.

Ice Mass Balance (IMB) buoys measure thermodynamic fluxes in the mass balance of sea ice floating in the Arctic (Figure 1b; Table II). IMBs are equipped with a thermistor string 3 m above sea ice, with an accuracy of 0.1˚C. Thus, IMBs measure in-situ T_a in offshore regions. Two IMBs (2013F and 2013G) were found floating inside of the three Beaufort Sea images when the satellite images were taken. Data were downloaded from Cold Regions Research and Engineering Laboratory (Perovich et al., 2013).

Ice-Tethered Profiler (ITP) buoys also float in sea ice, focused on seawater properties in the water column up to 800 m below the sea surface (Figure 1b and 1c; Table II). ITPs measure temperature of water 6 m below the ice/ocean interface and are telemetered to Woods Hole Oceanographic Institution in real-time. ITPs are different than IMBs because they measure water temperature 6 m below surface, instead of air temperature (Figure 1c). Thus, ITP data do not reflect T_a. ITP data are expected to give a slightly higher temperature than an air temperature monitor because (for most of the year) water is relatively warmer than air in the Arctic. However, in the Arctic, the mixed layer is at least 10 m deep. Thus, the ocean temperature measured by ITPs is approximately equivalent to the sea surface temperature, and thus can act as an additional tool to measure T_s of water. From here on, ITP data will be denoted as a measurement of T_a, however, it is more likely representative of T_s. It is important to note that limited ITP data overlap with Landsat 8 images in the Beaufort region (Figures 2 and 3).

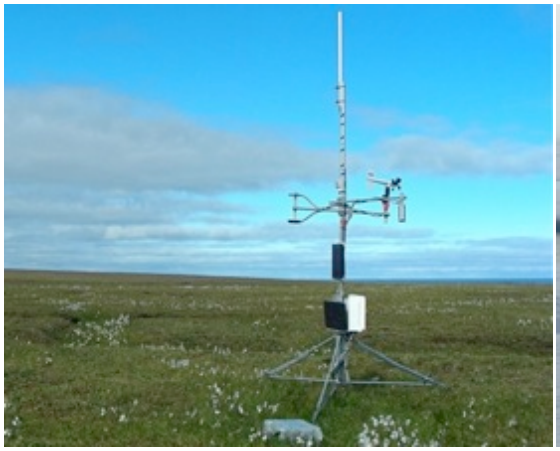

Figure 1a. Camden Bay land station in the summer (www.pubs.usgs.gov).

Figure 1b. IMB thermistor string in the distance, where temperature is measured 3 m above surface; ITP buoy is yellow in the water in the foreground (www.WHOI.edu).

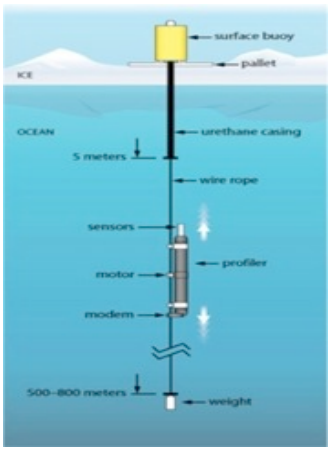

Figure 1c. Schematic drawing of an ITP buoy. Temperature measurements from 6 m below the ice-ocean interface are used in this study (www.WHOI.edu).

Figure 2. Map of the study region in Beaufort Sea on the Arctic coast of Alaska and Canada. The study region is enclosed by the center red rectangle. Satellite images are depicted in colored squares, numbered 1-28 chronologically. Meteorological land stations are black circles labeled A-O; the legend matches letters to station names. Floating buoys are in red teardrops. Note that not every satellite image has a station in it, in which case the closest station was used to find the in-situ T_a measurement.

Table I. Land Station Index

Letter	Location	Station	Latitude (degrees)	Longitude (degrees)	Altitude (m)
A	Point Hope	26623/PHO	68.5	-165.8	4
B	Cape Lisburne	PALU	68.9	-166.1	3.048
C	Point Lay	PPIZ	69.5	-163.2	7.0104
D	Wainwright	PATQ	70.5	-157.4	95
E	Barrow	BARROW	71.4	-156.5	0.9114
F	Teshekpuk Lake	KAKTESHE2	70.723	-153.83	7
G	Nuiqsut	PAQT	70.2	-151.1	11.872
H	Deadhorse	PASC	70.2	-148.5	11.872
I	Camden Bay	AK110	69.967	-144.76	3
J	Barter Island	PABA	70.1	-143.6	2.1336
K	Herschel Island	CWJN	69.6	-138.9	0.9114
L	Pelly Island	CWND	69.6	-135.4	6.096
M	Inuvik	CYEV	68.3	-133.5	67.9704
N	Cape Parry	CZCP	70.2	-124.7	85.9536
O	Sachs Harbour	CWSY	72	-125.2	88.0872

Table II. Floating Buoy Index.

Image	Location	Buoy	Latitude (degrees)	Longitude (degrees)	Altitude (m)
23	North Beaufort Sea	IMB2013F	76.5355	-139.4632	3
23	North Beaufort Sea	ITP72	77.1956	-148.3255	-6
24	South Beaufort Sea	IMB2013G	75.588	-141.8133	3
24	South Beaufort Sea	ITP68	75.5839	-141.7955	-6
24	South Beaufort Sea	ITP69	74.9234	-143.5716	-6
25	North Beaufort Sea	IMB2013G	75.4163	-147.7789	3

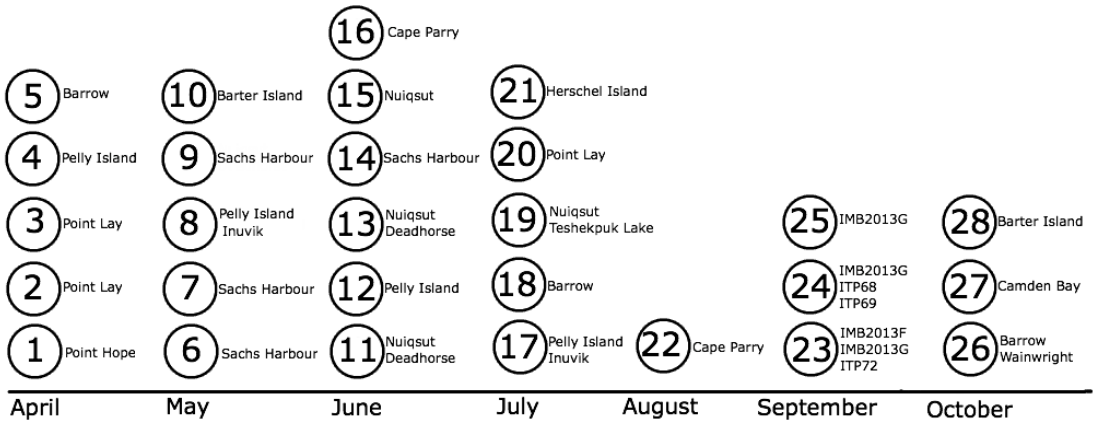

Figure 3. Map showing the image numbers in circles, associated with the closest air station during each month. This study heavily emphasizes April, May, June and July. All three satellite images in September are of the central Beaufort Sea, thus floating buoys are used to measure air temperature. Few images, such as 4 and 9, have two land stations because two stations are located in the exact satellite images coordinates.

h. Principles of the Study

For most accurate results, land and clouds were masked out of the image before the unsupervised classification was performed (Figures 4b, 5b and 6b). T_s varies depending on the skin surface type, therefore knowing surface type is crucial. Skin temperatures and albedo were calculated for each individual class, averaged over the whole satellite scene (Figures 4c-d, 5c-e and 6c-d). Thus, each satellite image had an averaged T_s and albedo for the water class, the melt pond class and the ice class. It is important to note that the calculated T_s and albedo that are averaged over the whole satellite scene were just of the sea ice, water and melt ponds, and not the land. All coastal satellite images included land, however, this study masked out land in order to only focus on sea ice (Figure 5d).

Not all satellite images had corresponding in-situ air temperature stations in the image. In cases without, the closest in-situ station was determined based on location coordinates (Figures 2 and 3). First, T_s and T_a were compared, using the average T_s of the whole image. Then, each satellite image was separated into three classes: water, melt ponds and ice. For the remainder of the study, T_a was compared and correlated to T_s, where T_s was averaged for the whole satellite scene for each class. The T_s was then compared to the closest in-situ T_a measurement.

When a station or buoy exists in an image, the temperature at the exact coordinate of the station was noted (Figures 2 and 3). When T_s and T_a are compared "at station", only the T_s from the exact location of the in-situ air temperature station is compared to the in-situ T_a. At land stations, the T_s "at station" measures the temperature of land surface, not water, sea ice or melt ponds. This "at station" T_s is not considered unless "at station" is specifically mentioned.

Some images have multiple in-situ stations, thus the multiple T_a were considered and compared to provide more data. For example, image 26, taken on October 6, compares T_a from both Barrow and Wainwright to satellite-derived T_s (Figure 3). Both of these comparisons were used when "at station" was mentioned. Data from both stations were included, comparing the same averaged T_s of each class to the different T_a. When an image

had multiple in-situ stations, it had multiple points on a graph. Multiple stations were included whenever possible to improve the quantity of data in an already limited coastal Arctic region.

The same methodology applied to albedo calculations. Albedo was averaged for the whole scene for each class, and then compared to satellite-derived and averaged T_s.

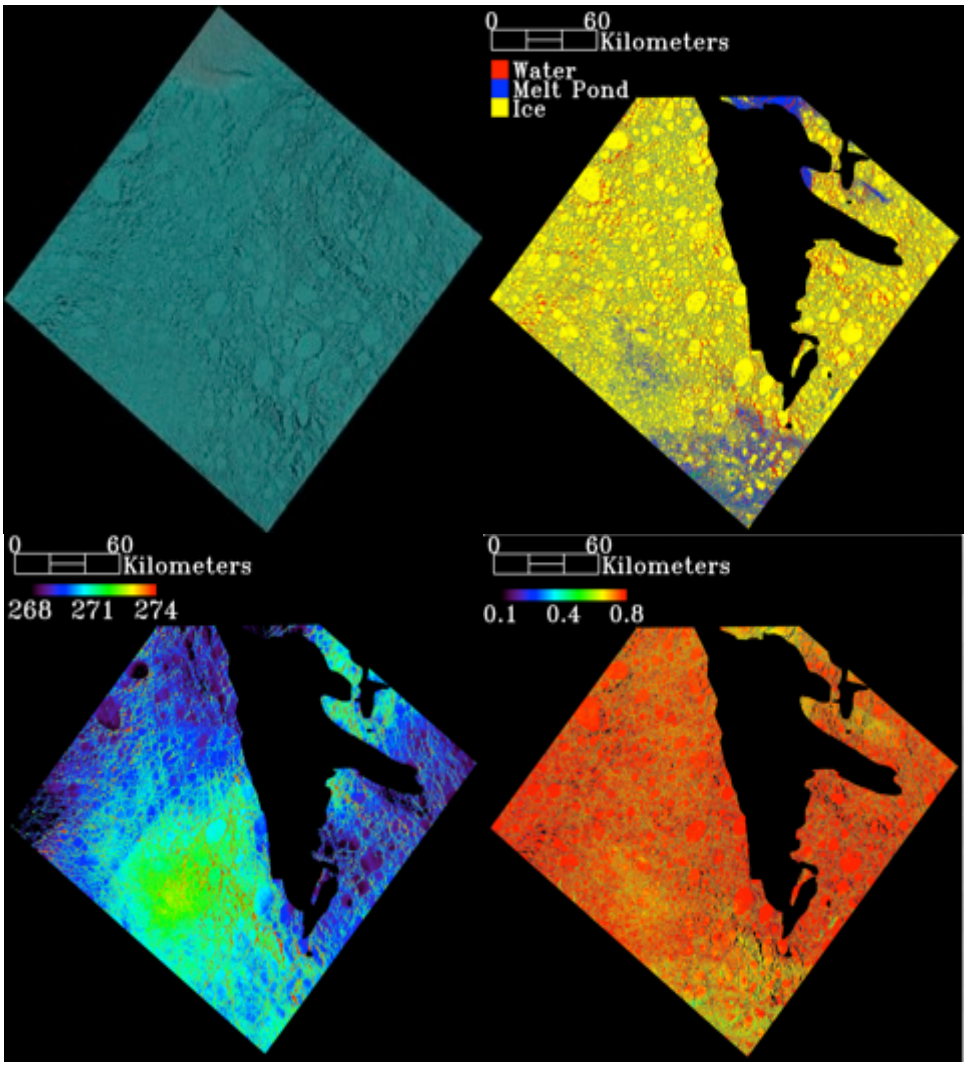

Figure 4a (left). A true color image of a sea ice scene in the middle of the Beaufort Sea on Sept 1, 2013 (www.earthexplorer.usgs.gov). Note low-lying clouds in the upper corner. The following three images are products of this scene.

Figure 4b (right). A classification image of the scene with low-lying clouds in the upper corner and cirrus clouds masked out, appearing as black in the center of the image. Water appears red, melt ponds are blue and ice is yellow.

Figure 4c (left). A rainbow false color image of T_s, showing colder regions as blue and warmer regions as green/red. Cirrus and low-lying clouds are masked out.

Figure 4d (right). A rainbow false color image of satellite-derived albedo, where lower albedos are black and blue and higher albedos are red and yellow. Note that colder regions (Figure 5c) have higher albedos, and warmer regions have lower albedos.

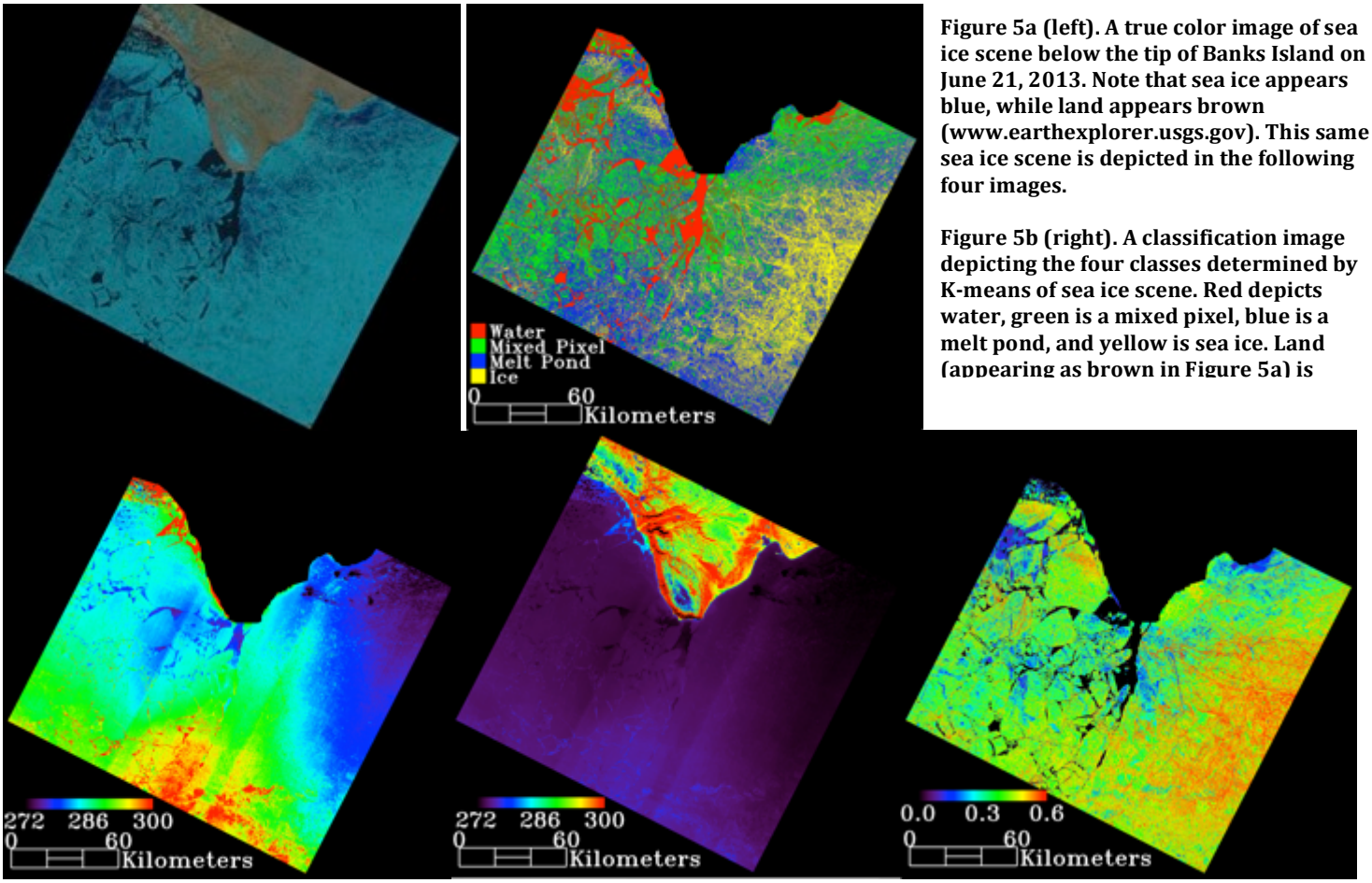

Figure 5a (left). A true color image of sea ice scene below the tip of Banks Island on June 21, 2013. Note that sea ice appears blue, while land appears brown (www.earthexplorer.usgs.gov). This same sea ice scene is depicted in the following four images.

Figure 5b (right). A classification image depicting the four classes determined by K-means of sea ice scene. Red depicts water, green is a mixed pixel, blue is a melt pond, and yellow is sea ice. Land (appearing as brown in Figure 5a) is

Figure 5c (left). A rainbow false color image of satellite-derived T_s, where colder regions are purple and blue, warmer regions are green and yellow, and hottest regions are yellow and red. Land is masked.
Figure 5d (middle). A T_s image including land to show the temperature difference between land and sea.
Figure 5e (right). A rainbow false color image of satellite-derived albedo, where regions with the lowest albedo appear black and blue, while highest albedos appear yellow and red. Land is masked. Note that regions of high sea ice density have high albedo.

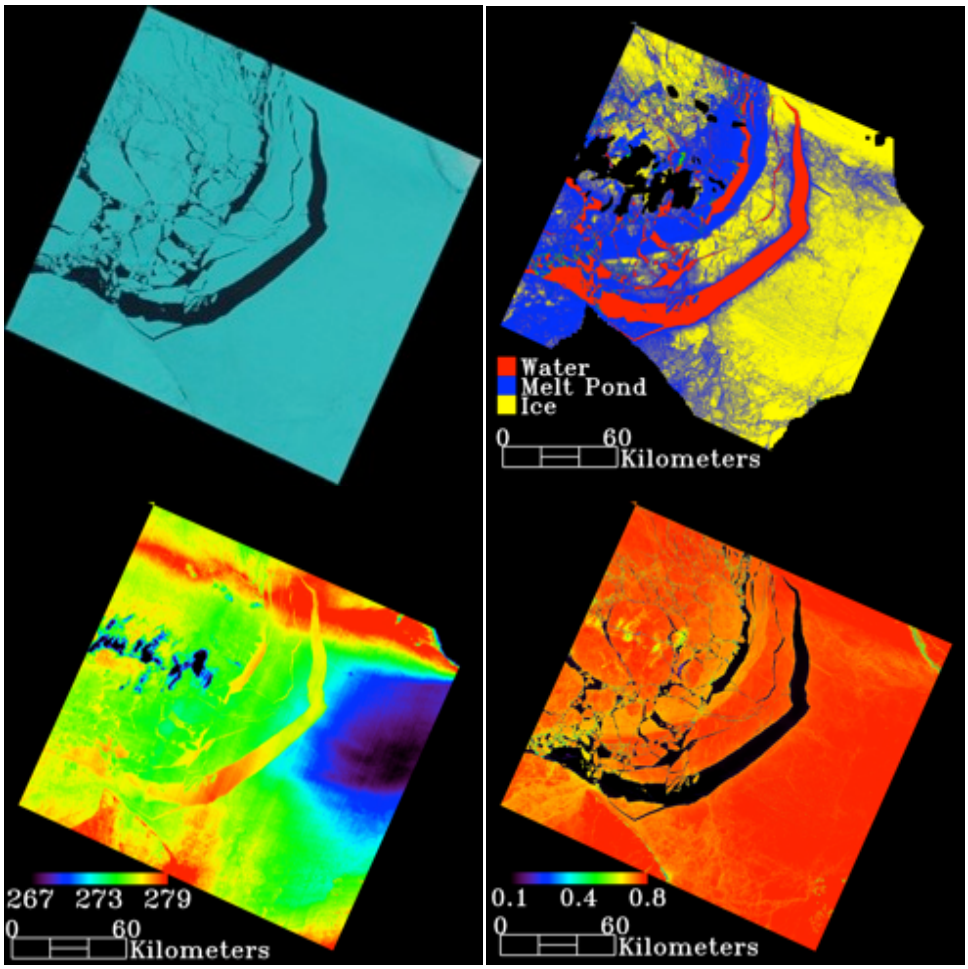

Figure 6a (left). A true color image of landfast ice breaking away from Sachs Harbour on May 18, 2013 (www.earthexplorer.usgs.gov).

Figure 6b (right). A classification image of the scene with land and clouds masked out, appearing as black.

Figure 6c (left). A rainbow false color image of T_s with clouds masked out. Warmer regions appear red and yellow, while colder regions appear green and blue.

Figure 6d (right). A rainbow false color image of albedo, where higher albedos appear red while lower albedos appear yellow, and lowest albedo is black.

3. Results

a. Understanding the relationship between T_s and T_a

T_s and T_a are measured differently: T_s refers to the surface skin temperature measured by satellites capturing upwelling longwave radiation; T_a is measured by land stations 3 m above ground surface and IMB buoys 3 m above ice surface. ITP buoys are included as an in-situ measurement; however, they measure the temperature of the water 6 m below the surface (Figure 1c). Because the top 10 m of the Beaufort Sea is relatively well mixed, the measured sea temperature is equivalent to the sea surface temperature, and thus is more closely correlated to T_s than T_a of water. In this study, T_a data come from all three in-situ sources, however, each source is depicted as different colors on the graphs: land stations are red, IMBs are pink, and ITPs are purple.

Satellite-derived T_s and in-situ T_a in the same region were related, though have different magnitudes. T_s was measured at the exact longitude and latitude of the in-situ T_a monitors (Figure 7). For a majority of the comparisons, the surface type was land, not sea ice, since the coastal in-situ air temperature stations are located on land. The difference between T_s and T_a ($T_s - T_a$), on average, varied by 3.5˚C (Figure 7). For example, Sachs Harbour on April 24 (image 5, [see Figure 2]) had an air temperature of -2.2˚C, while the skin temperature of the land station was 1.81˚C. However, some T_s and T_a measurements from the same region at the same time varied greatly: Nuiqsut on June 26 (image 15) had an air temperature of 15.6˚C and a skin temperature of 26.6˚C, a difference of 10˚C.

Jin and Dickinson's study (2010) showed that in the mid-latitudes, $T_s - T_a$ for land at noon was 15˚C, but only 3˚C at night. During the day, the positive $T_s - T_a$ difference was driven by solar insolation and decreased plant evotransporation; nighttime $T_s - T_a$ was driven by longwave radiation balance, with T_s usually higher than T_a (Prigent et al., 2003). However, snow-covered regions, including Greenland and Antarctica, were measured to have small diurnal ranges, less than 5˚C (Jin & Dickinson, 2010).

T_a and satellite-derived T_s had a coefficient of determination of 0.74 when measuring the T_s at the exact coordinate of the in-situ T_a station (Figure 7). By removing outlier Nuiqsut data, the skin temperature and air temperature correlation improves to 0.828.

The rest of this paper focuses on surface types of ice and water in the Beaufort region, rather than land surfaces.

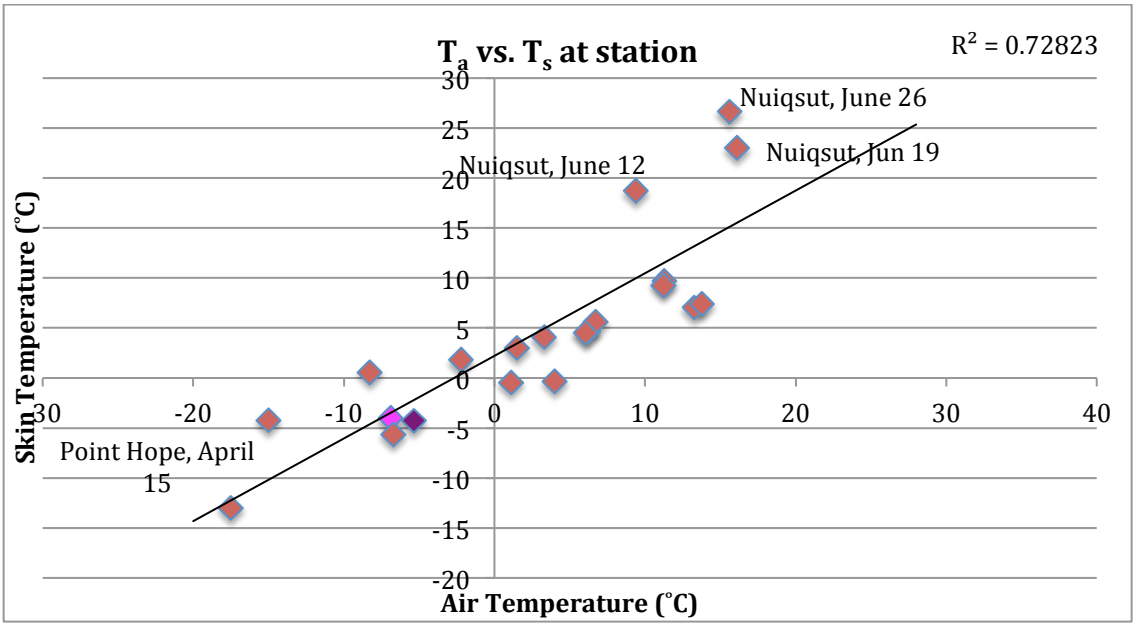

Figure 7. A graph depicting the correlation between T_a and satellite-derived T_s at the in-situ stations. Land meteorological stations are in red, IMB data are in pink, and ITP data are in purple. Note that ITP buoys do not directly measure T_a and are more likely to represent T_s. Major outliers are labeled with the name of the station and date.

b. Outlier Data

T_a is affected when meteorological stations have a high altitude above the surface, and if high winds are present. High elevation stations may measure T_a above the surface boundary layer, causing a greater difference between T_a and T_s (Table I). High winds will lower the T_s, also causing discrepancy in temperatures.

The land station in Nuiqust station consistently measures suspect data. In Figure 7, the three largest outliers are Nuiqsut in June. Nuiqsut has an elevation of 11.88m and wind never exceeded 10 m/s when satellite images were taken (Table I). It is unclear what caused the anomalous values, however, stations in the Arctic sometimes break down from

the harsh climate. It is possible that Nuiqsut needs to be recalibrated to measure better T_a. By removing the Nuiqsut outliers, the correlation increased from 0.73 to 0.83. From here on, all Nuiqsut data have been removed from the analysis.

c. Averaged T_s vs. T_a

Since T_a varies relatively little (compared to T_s) over large areas, T_a was then compared to the average T_s of the whole satellite scene. The average T_s takes into account all surface types, reflecting the average T_s of a 200 km by 200 km region. At any given point, the T_s of water and sea ice will vary greatly; but by averaging the whole satellite scene T_s, the averaged T_s may be most closely correlated with T_a.

T_s averaged over the whole Arctic scene, encompassing all surface types, had a correlation determination of 0.788 (Figure 8). This correlation was strong, suggesting that T_s and T_a are closely linked. $T_s - T_a$, had a standard deviation of 3.4˚C, where the average T_s of a whole Beaufort sea ice scene had a mean $T_s > T_a$ by 0.56˚C.

By examining each surface type's correlation with T_a, we can better understand the relationship between the two temperatures.

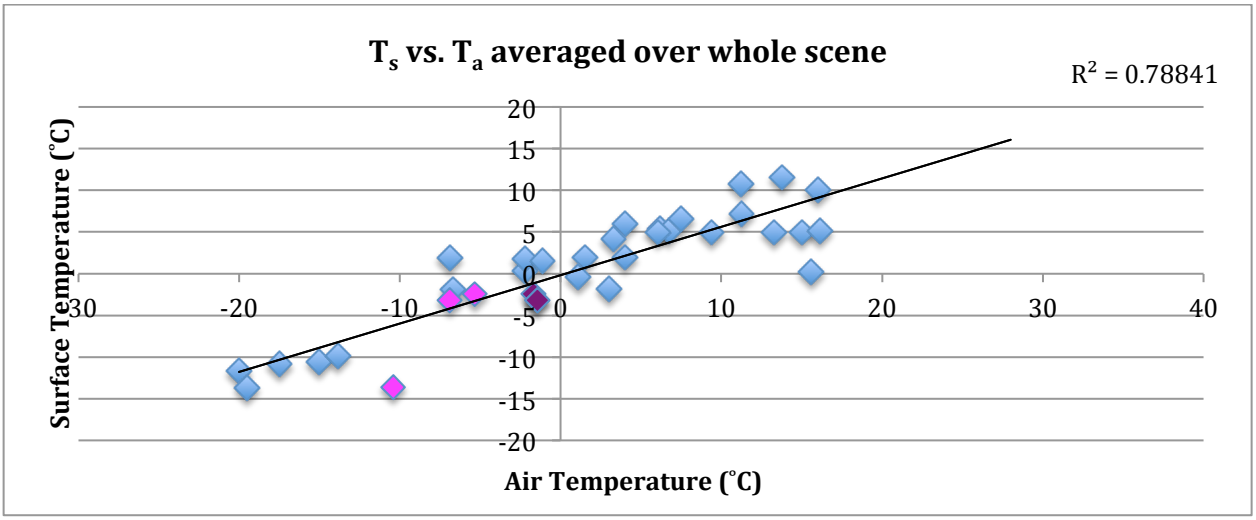

Figure 8. Each dot on this graph represents T_s averaged over a whole satellite scene compared to in-situ T_a from the closest land (or buoy) station. Some scenes have two dots on the graph because two in-situ stations are located in the satellite image. ITP data appear pink; IMB data appear purple. The coefficient of determination is 0.788.

d. Surface Type Matters

A major strength of Landsat 8 is that its high resolution allows for analysis of individual surface types. One pixel is 30 m by 30 m and one image covers an approximate scene size of 170 km north-south by 185 km east-west. The Arctic is thin with meteorological land stations, so not all satellite images had in-situ temperature gauges in the image (Figures 2 and 3). Thus, T_a was compared to T_s measured across 31,450 km^2. T_a stays uniform across large areas, however, T_s varies greatly depending on surface type. Therefore, surface type matters when comparing T_s and T_a.

Understanding the surface type is important, as T_s varies depending on the specific surface (Jin & Dickinson, 2010). Surfaces respond quickly to solar forcings, and thus surfaces warm with the rising sun; absorbed radiation at the surface depends on surface type since albedo decreases with vegetation density (Prigent et al., 2003). Vegetation influences T_s because soil moisture is correlated with evaporation rates, which influence heat flux driven by $T_s - T_a$ differences (Prigent et al., 2003). While surface types in the Arctic have less significant impacts from evotransporation, surface type plays a major role in $T_s - T_a$ difference because albedo and skin temperature vary greatly between sea ice and open water.

Four classes were determined using K-means unsupervised classification. The well-defined spectral signatures separated surfaces into pure water, pure ice and two classifications of mixed pixels (Figures 4b, 5b, and 6b).

Satellite-derived T_s was calculated for each classification (Figures 4c, 5c and 6c). Pure water had the highest T_s, compared to the other three classes, ranging from 11.76˚C to -9.98˚C. T_s of melt ponds ranged from 6.93˚C to -14.33˚C. T_s of ice ranged from 6.67˚C to -14.14˚C. All four classes ranged in T_s between 20.09˚C (water), 20.82˚C (ice) to 21.27˚C (melt ponds). Thus, not one class had significantly more variability than the other. It is important to note that some water temperatures were lower than its freezing point of -1.8˚C. Likewise, sea ice was too warm, greater than 0˚C. Full discussion of possible sources of error is presented in section 2f.

No study has specifically linked surface types in the Arctic with T_s. However, Jin and Dickinson (2010) included "snow and ice" cover type in a MODIS study, finding that the monthly mean T_s of "snow and ice" over the globe was -40.2˚C in April, -42.3˚C in July, and -36.08˚C in October. These monthly T_s averages are much lower than T_s results from the Beaufort region; T_s in July should be warmer than April, as snow and ice melt in the summer. In this study, the Beaufort's average T_s of ice in April was -11.55˚C, 5.39˚C in July, and -2.61˚C in October. Skin temperatures can vary yearly; Jin and Dickinson's study was conducted in 2010, while this study measured T_s in the Beaufort region in 2013, however, general trends should indicate that T_s of ice is colder during the beginning and end of melt season and warmer during the peak of melting.

T_s was then compared to in-situ T_a from the nearest land station or buoy (Figure 3). It is important to note that T_s was averaged over the whole satellite scene for each class, and then compared to the closest in-situ station, which in some cases did not overlap perfectly with the coordinates of the satellite scene. Water had the lowest coefficient of determination between T_s and T_a, at 0.772 (Figure 9a). Melt ponds had a coefficient of 0.887 (Figure 9b). Ice had the highest coefficient of determination at 0.889 (Figure 9c). With consistently high coefficients of determination between T_s and T_a for water, melt ponds, and ice, there must be a strong relationship between the two types of measured temperature.

These results are consistent with literature of T_s and T_a coefficients of land types in lower latitudes. Prigent et al.'s study (2003) found a coefficient of determination of 0.88 over the globe over a year; Vogt et al.'s study (1997) found a coefficient of 0.823 in Andalusia, southern Spain.

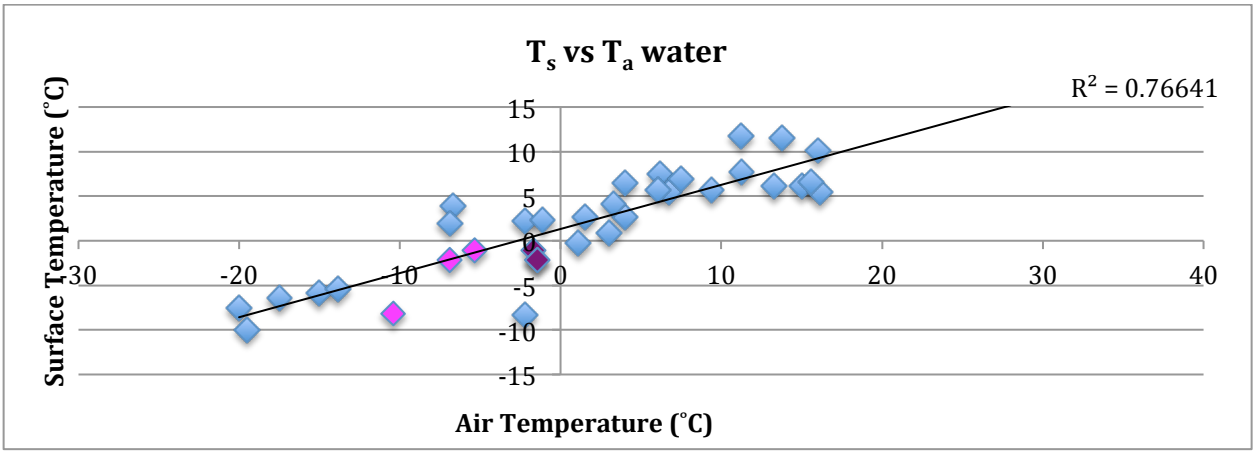

Figure 9c. Air temperature plotted against skin temperature for pixels classified as water. Purple points represent data from ITPs; pink represents data from IMBs. The correlation coefficient is 0.766.

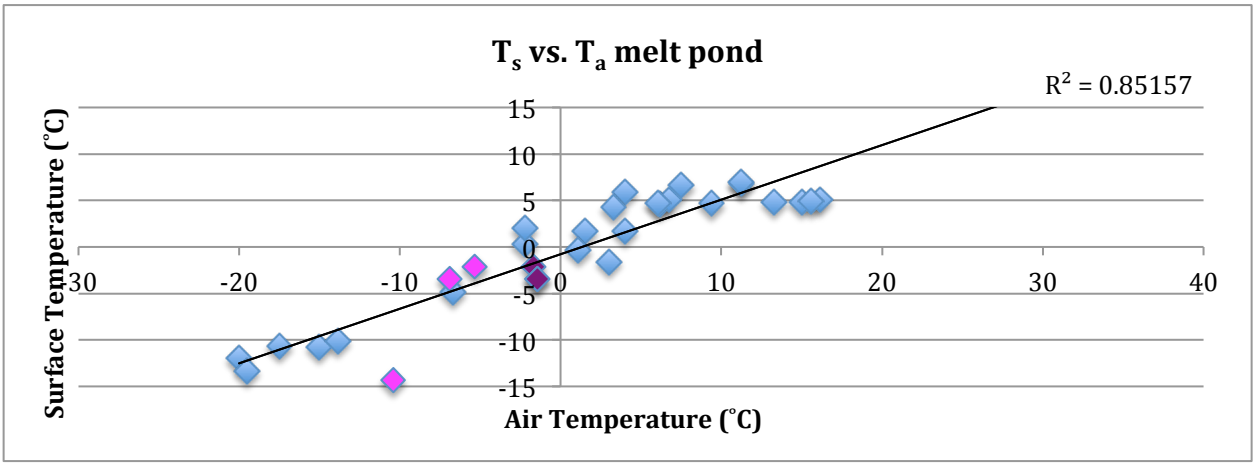

Figure 9b. Air temperature plotted against skin temperature for melt ponds. Purple points represent data from ITPs; pink represents data from IMBs. The correlation coefficient is 0.852.

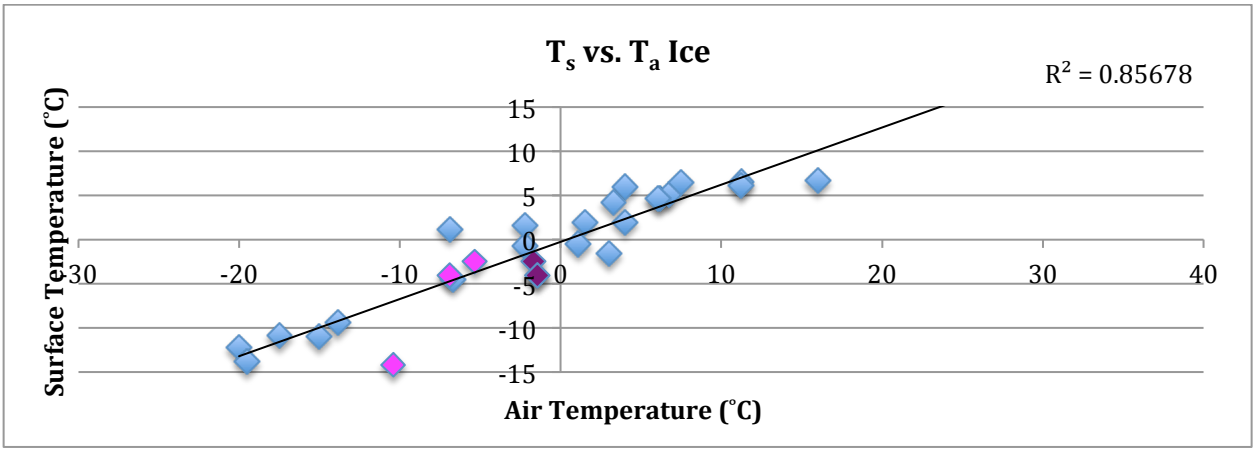

Figure 9b. Air temperature plotted against skin temperature for pixels classified as pure ice. Purple points represent data from ITPs, pink represents data from IMBs. The correlation coefficient is 0.857.

e. Seasonal Variability

There is a well-defined seasonal cycle for the variation of $T_s - T_a$ in the Beaufort region (Figure 10). The maximum positive deviation from zero was observed in April and October, with deviations up to 12˚C in April over water. The maximum negative deviation from zero was in July, peaking at -6.3˚C, during melting season. Note that this study does not encompass the full seasonal cycle because of the limited well-lit time frame, and only focuses on the melt-season cycle from onset in April to peak melt in middle of the summer, to freeze-up in September and October (Figure 10).

At the beginning of the melt season, $T_s > T_a$ (Figure 10). The sun rises in the Arctic on March 21, thus during April and May, the surfaces warm faster than the air because surfaces respond quicker to solar forcing changes (Prigent et al., 2003). During the peak melting season, from June to August, $T_s < T_a$ (Figure 10). In the summer, air temperatures increase dramatically, from -40˚C to 30˚C in some areas. As sea ice warms and begins to melt, it releases heat into the surrounding air, causing T_a to increase. During freeze-up, $T_s > T_a$, reflecting that air temperatures begin to cool as winter approaches, while surface temperatures stay relatively warmer, responding to solar forcings.

All surface variations follow the same seasonal cycle of $T_s - T_a$ (Figure 10). Water had the largest range in $T_s - T_a$. T_s of water was measured to be as cold as -9.986˚C on April 17 (image 4), which is colder than the freezing point of seawater. The T_s was influenced by the presence of sea ice, which affected the $T_s - T_a$, further explained in Section 2f. Water T_s increased as high as 11.768˚C on July 13 (image 21), from absorption of incoming radiation with the expansion of leads and open water.

T_s of melt ponds similarly follows patterns of the T_s of ice. Melt ponds and ice have similar spectral signatures; melt ponds are identified as mixed pixels with a higher fraction of ice than water. Thus, the skin temperatures are closely aligned, with melt ponds having a slightly warmer T_s in all months compared to ice because it takes into account the relatively warmer water on top of ice (Figure 10).

The seasonal cycle is dominant, even though satellites and in-situ stations are spaced throughout the entire Beaufort region, along the Alaskan and Canadian coast and in the center of the Beaufort Sea (Figure 2).

Literature on seasonal variability of $T_s - T_a$ is scarce. The seasonal cycle of $T_s - T_a$ in mid-latitudes has a lower deviation from mean than in higher latitudes of 54°N (Prigent et al., 2003). No study has measured in latitudes as high as the Arctic.

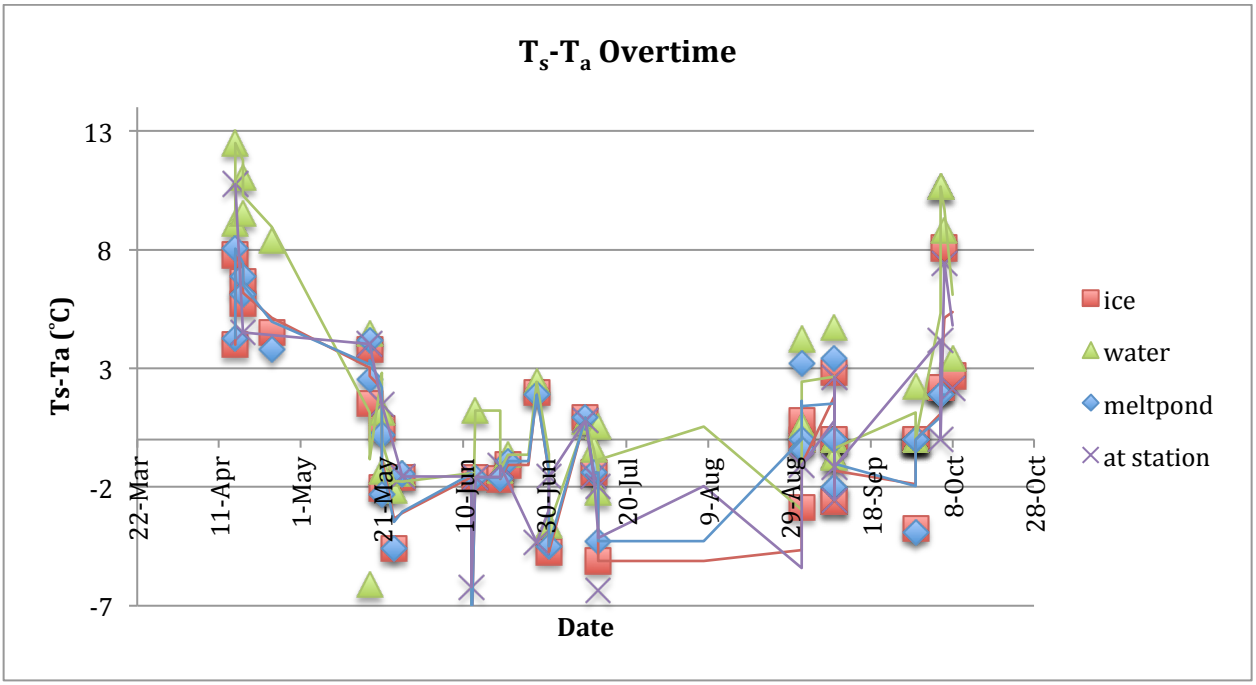

Figure 10. $T_s - T_a$ during the summer months in the Arctic, from April to October. $T_s > T_a$ during the onset of melting and freeze-up. $T_s < T_a$ during melting in the middle of the summer. Outlier data from Nuiqsut are not included. All surface types are shown, as well as "at station" data.

f. Albedo

Albedo measures the reflectivity of a surface. Arctic sea ice acts as a blanket for the planet's heat budget, as its high albedo reflects incoming radiation back to space. As ice melts during the summer, open water becomes more prominent; with water's lower albedo, incoming radiation is absorbed, causing water to heat up and melt nearby ice. This process is self-sustaining, leading to an ice-albedo feedback cycle. As ice melts at an accelerating rate in the Arctic, it is important to monitor surface albedo.

Figure 11. Melt ponds can be centimeters deep, as shown in light blue on left side of image, or meters deep, shown on right side of image. Depth of melt pond greatly affects surface albedo (www.nasa.gov).

Melt ponds range from centimeters to meters deep, and thus the albedo of melt ponds vary greatly (Figure 11). In this study, albedo for melt ponds ranged from 0.299 to 0.688, with an average of 0.51, encompassing all stages of melt pond development: melting ice, blue water and deep melt ponds (Figure 12); spectrometers measure their albedos to be 0.53, 0.28, and 0.21, respectfully (Grenfell & Perovich, 1984), consistent with these data. As surface temperatures increase throughout the summer, ice melts to form blue ice and melt ponds, changing surface albedo dramatically.

The albedo for ice ranged from 0.414 to 0.786, with an average of 0.58 (Figure 12). Ice had the greatest variation, however, 60% of results ranged within 0.6 to 0.8 (Figure 12). These results are consistent with spectrometers, which measure bare ice to have an albedo of 0.43, and snow-covered ice to have an albedo of 0.77 (Grenfell & Perovich, 1984); some studies measure albedo of bare ice to be higher, at 0.5, and snow-covered ice to have an albedo of 0.9 (National Snow and Ice Data Center, 2013). Surface albedo rises with an increase in white reflective surfaces (ice) and decreases with the presence of darker surfaces (water). The ice pixels in these satellite images are not split into separate categories of bare ice and snow-covered ice, thus the albedo ranges greatly.

The albedo for water ranged from 0.023 to 0.254 (Figure 12). Under perfect conditions, spectrometers measure water to have an albedo ranging from 0.06 to 0.08 (Grenfell & Perovich, 1984). The higher albedo measured for water pixels is explained by the presence of ice, which increases the albedo higher than expected. Refer to the Section 2f for explanations for anomalously high or low albedos.

g. T_s Correlated with Albedo

There have been no studies directly linking albedo and temperature in the Arctic. Studies have shown that they are related in the feedback dynamics, but have not specifically

written on the relationship in context of Arctic sea ice. Regions of high ground temperature tend to correlate with regions of lower albedo (Køltzow, 2003). Køltzow's study (2003) also determined that the daily cycle of albedo follows that of the daily temperature cycle: albedo peaks and falls together with surface temperature, indicating a relationship. Further, T_s is partly determined by surface albedo (Jin & Dickinson, 2010) and thus their relationship is important to investigate.

T_s and albedo are correlated over identical regions in the Beaufort Sea (Figures 5c and 5e) Albedo was calculated and averaged over each satellite scene, and then compared to the averaged surface temperature for each class (Figure 13). ITP data was included only in the water class because ITPs more closely measure T_s than T_a, and thus can provide an additional T_s measurement (Figure 1c).

T_s and albedo of water had the highest correlation, with a coefficient of determination of 0.595; ice had a correlation of 0.522 and melt ponds had a correlation with 0.487 (Figure 13). In general, higher T_s was correlated with lower albedos, and lower T_s was correlated with higher albedos, agreeing with Køltzow's (2003) results.

Melt ponds had the highest degree of variability, as the class represents all stages of a melt pond. In Figure 12, melt ponds are represented in blue and have the greatest variation. Cold melt ponds tend to clump closer to the ice class, while warmer melt ponds clump closer to the water class. A cold melt pond is shallower, allowing ice to strongly affect its temperature, correlated with a higher albedo. Warmer melt ponds are deeper ponds with a similar spectral signature to that of water, thus its low albedo is closely linked to the albedo of open water (Figure 11).

The errors in classifications found with T_s were also apparent in albedo. Water T_s below -2˚C tended to have a higher albedo of 0.2, which followed the same pattern of the albedo being altered by the presence of ice (Figure 12). Similarly, high ice temperatures near 10˚C had lower albedos of 0.4, suggesting that water lowered ice's apparent albedo (Figure 12). Explanation for anomalously high and low albedos is further discussed in Section 2f.

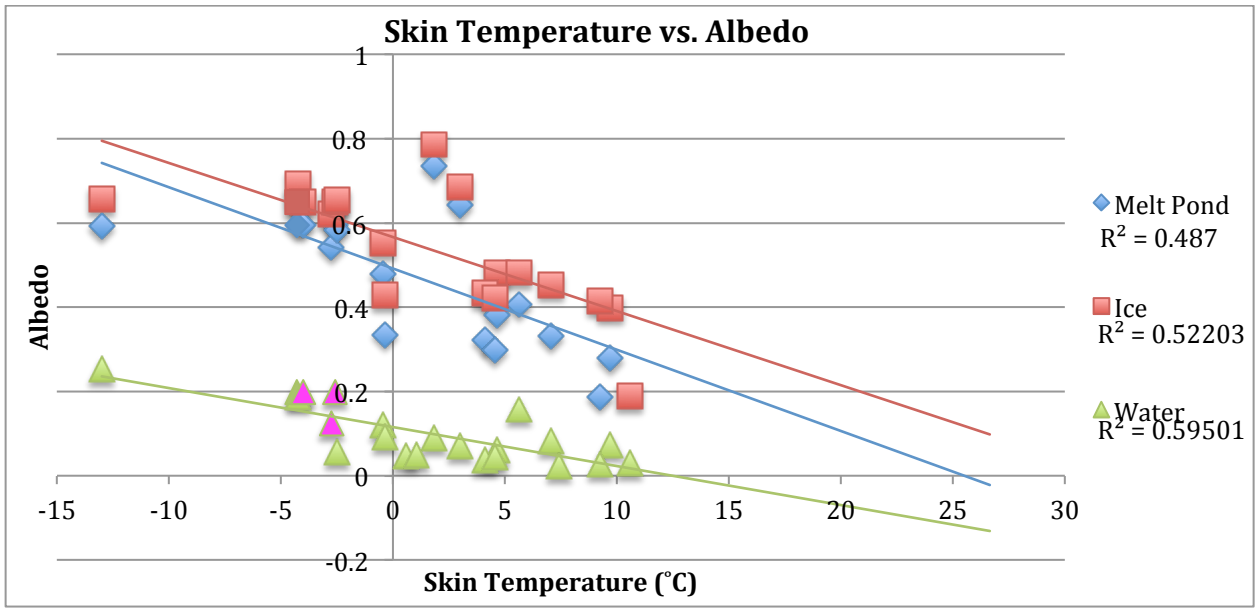

Figure 12. T_s of different surface types and their correlation with albedo. Ice is shown in red, water in green, and melt ponds in blue. ITPs are colored pink and displayed for water class only, as ITPs are closely correlated to T_s. Correlation coefficients are given. Water may obscure the ice temperature, producing ice Ts above 0˚C; similarly, ice may obscure water, giving water temperatures below -2˚C (as discussed in Section 2f).

h. T_s and Albedo Seasonal Cycle

There was a seasonal progression of surface albedo (Figure 13a-c). Albedo was high during on-set of melting, low during the peak melting season, and then high again during freeze-up across all variations of surface types. Albedo of ice plays a crucial role in determining the Earth's heat budget. As ice melts, incoming radiation is absorbed rather than reflected by surfaces with lower albedos, increasing temperatures. This leads to further ice-melt, causing an ice-albedo feedback.

T_s and albedo had opposite phase changes (Figures 13a-c). Albedo tended to be high during the onset of melt season because the T_s was low and scenes were covered by sea ice, with an albedo of 0.6 to 0.8. The albedo then decreased in the summer months when temperatures increased causing ice to melt and melt ponds to deepen. When sea ice melts to water, the water absorbs the incoming radiation, rather than reflects it, starting the ice-albedo effect. This lower albedo and heightened surface temperature will increase air temperatures, causing more ice melt. When air temperatures finally decrease, causing surface temperatures to decrease, melt ponds and open ocean freeze to form sea ice in

September and October. These results are consistent with albedo studies of Arctic sea ice (Perovich, 2002).

Perovich (2002) determined that there are five distinct phases of albedo evolution during the summer melt months: dry snow, melting snow, pond formation, pond evolution, and fall freeze-up. This study is in agreement, showing that the pure ice had an albedo around 0.7, albedo of melting snow decreased to 0.6, then ponds began to form with an albedo of 0.5, as ponds deepened, albedo lowered to 0.42, and then during fall freeze-up, albedo began to increase from 0.42 to 0.63 (Figures 13a-c). Albedo of ice was highly affected by temperature. Since albedo of pure ice is determined by air bubbles in ice, even a few centimeters of snow or meltwater on top of ice can "hide" the albedo of ice altogether (Allison et al., 2003).

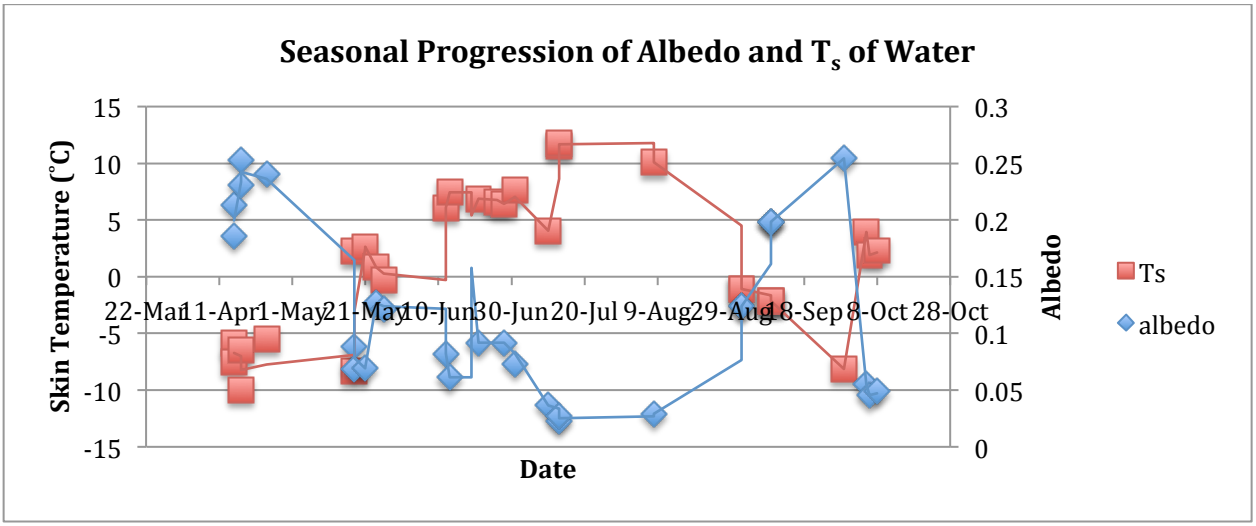

Figure 13a. Albedo and skin temperature of water pixels overtime. Albedo is shown in blue, while T_s is in red. Albedo decreases throughout melt season, and increases during fall freeze-up slightly, varying from 0.06 to 0.2; skin temperature decreases from 10°C in spring to almost -15°C in the middle of melt season, and then rises back to 10°C by fall freeze-up.

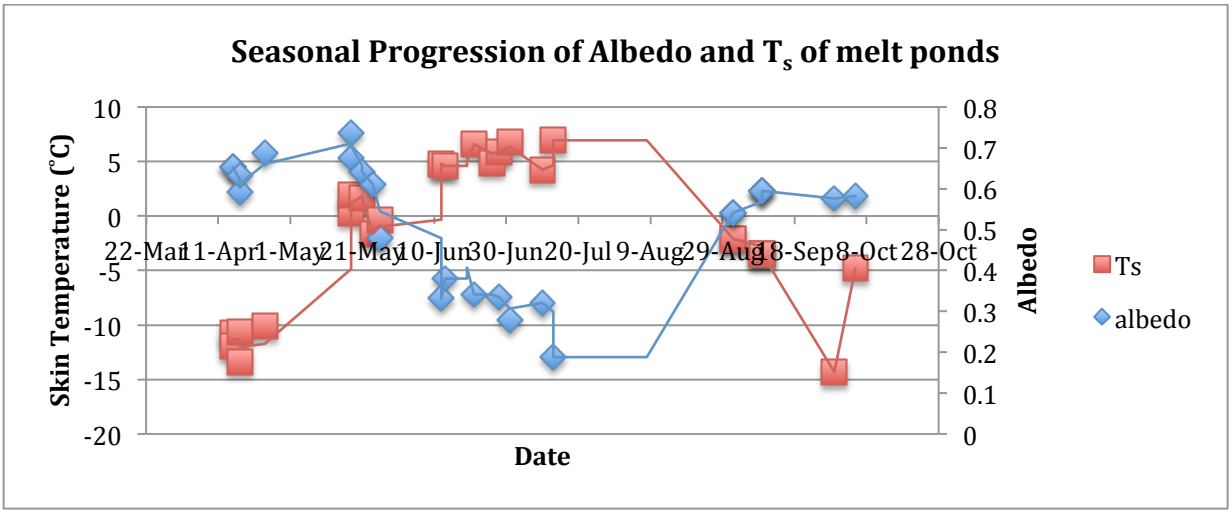

Figure 13b. Albedo and T_s of ice between April and October. Albedo is in blue; T_s is in red. Albedo before melt is 0.6, due to fact that in April, these ponds are outliers and albedo measured is really that of pure ice. During the melt season, the albedo is between 0.4 and 0.2, varying depending on depth of melt ponds. In September and October, during freeze-up, albedo increases again to 0.6, reflecting the fact that these melt ponds are indeed freezing and becoming pure ice.

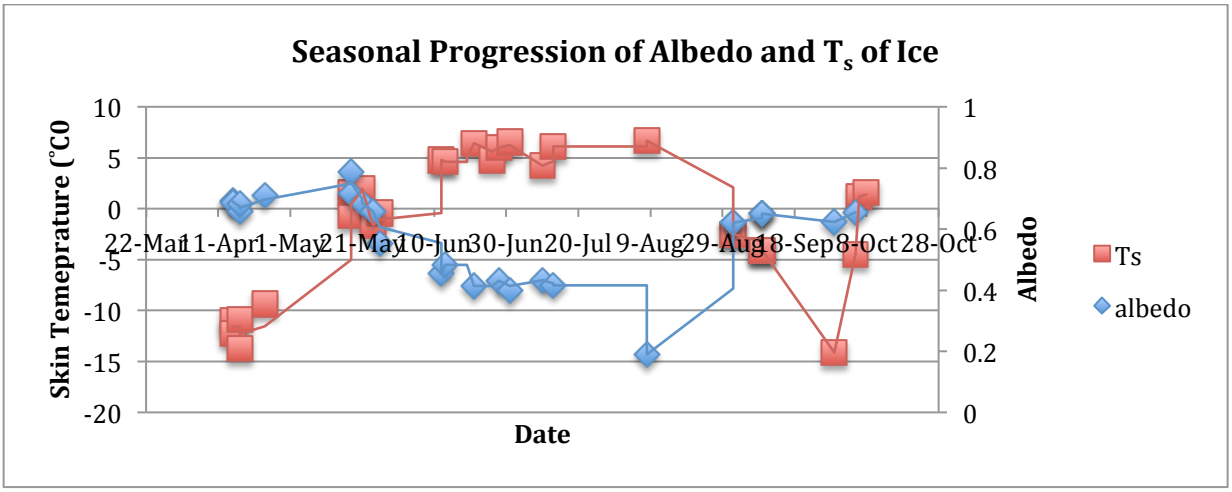

Figure 13c. Albedo and T_s of melt ponds from April to October. Albedo is in blue, T_s is in red. Albedo of ice is about 0.6 before and after melt, and decreases to 0.5 during melt. Skin temperature increases from around -15°C before melt to 5°C during melt, and then decreases again during freeze-up.

It is important to note that water underwent a change in albedo in this study (Figure 13a). In April and September, the average albedo of water was 0.22, however, in June and July, albedo decreased to 0.07 (Figure 13a). One reason for the major fluctuations in water, when the albedo should stay consistent, is because the satellite images were taken from all over the Beaufort Sea region, rather than the same location (Figure 2). April images were taken from the northwest coast of Alaska, near the Chukchi Sea. September images are taken from the center of the Arctic, where a majority of the scene was covered by sea ice, so

leads and polynas were classified as open water, resulting in a higher albedo (Figures 4b). Water albedo should consistently stay between 0.06 to 0.08. Small fluctuations are normal, however, major changes to 0.22 suggest that the albedo of water was enhanced by the presence of ice. Further details on sources of error for water classifications are explained in Section 2f.

These results are consistent with mid-latitude seasonal change of albedo and skin temperature. In mid-latitudes, albedo decreases from winter to summer, peaking in February and March, and then increases through spring and into winter; skin temperature has the opposite phase, where temperatures are low in winter, increase in summer to peak in July, and then cool down again until December (Jin & Dickinson, 2010).

i. Albedo and Sea Ice Thickness

There is also a correlation between ice thickness and albedo (Lindsay, 2001). Since albedo is a function of surface type, cloud cover, solar zenith angle, ice thickness and snow depth, albedo can be computed. As ice thickness increases on bare ice surfaces (no snow), albedo also increased (Lindsay, 2001). Ice thickness increases with ice age; the older the ice, the thicker it is, and thus the greater the albedo (Lindsay, 2001). Younger ice is typically thinner than older ice. In March 2012, 75% of the ice pack was dominated by first-year ice, increased from 58% in March 1988, thus suggesting a trend that Arctic sea ice will also have a lowering albedo.

j. T_s – T_a Proportional to Heat Flux

The difference between T_s and T_a is proportional to heat flux. In the Arctic, sea ice blankets the ocean, minimizing the heat exchange between the relatively warm ocean and the colder atmosphere. In the summer, sea ice melts allowing for heat to enter the atmosphere. Understanding heat flux is important because a small change is critical to ice thickness (Kwok & Untersteiner, 2011).

Heat flux describes the flux of sensible heat from a surface to the atmosphere above it. Heat flux is proportional to the drag coefficient (C_D), the heat capacity (C_P), wind speed (U), density (ρ), and change in temperature ($T_s - T_a$):

$$F_H = C_D C_P U \rho (T_s - T_a)$$

Air has a density of 1.2922 kg/m^3 at 0˚C, the heat capacity of air is 1.2 J/kg/K, and the average drag coefficient of rough ice is 2.8x10^{-3} (Prinsenberg & Peterson, 2002). Land stations measure wind speed, in addition to air temperature. Wind speeds range from 1.56 m/s to 11.31 m/s in the Beaufort Sea region during this study. All images are taken between 20:00 and 23:00 UTC, from April to October, thus winds are relatively calm. Winds do, however, vary and there are no direct patterns for certain locations to be windier than others along the Beaufort coast (Figure 14).

A positive temperature difference between the surface and the air indicates a positive heat flux. The heat flux from the ice to atmosphere ranged from about -300 W/m^2 to +650W/m^2 (Figure 15). In April and May, sun begins to shine in the Arctic, warming up the sea ice surface quicker than the air since surfaces respond quicker to solar forcings (Prigent et al., 2003). Thus, T_s lost heat to the atmosphere, resulting in a positive heat flux (Figure 14). In June, July and August, during the peak of the melting season, T_a increased more so than T_s. Thus, heat was lost from the atmosphere to the sea ice, resulting in a negative heat flux (Figure 15). It is expected that during the beginning of freeze-up in September and October, heat flux will return to positive, indicating that sea ice loses heat to the atmosphere. However, there are no September heat flux estimates since September satellite scenes are of the center of the Beaufort Sea and their corresponding in-situ buoys do not measure wind speed (Figure 3); future studies could use alternative wind products, discussed at the end of this section, for this purpose. Note that wind speed showed no apparent seasonal dependence (Figure 14), thus the seasonal cycle in heat flux is driven by $T_s - T_a$ (Figure 15).

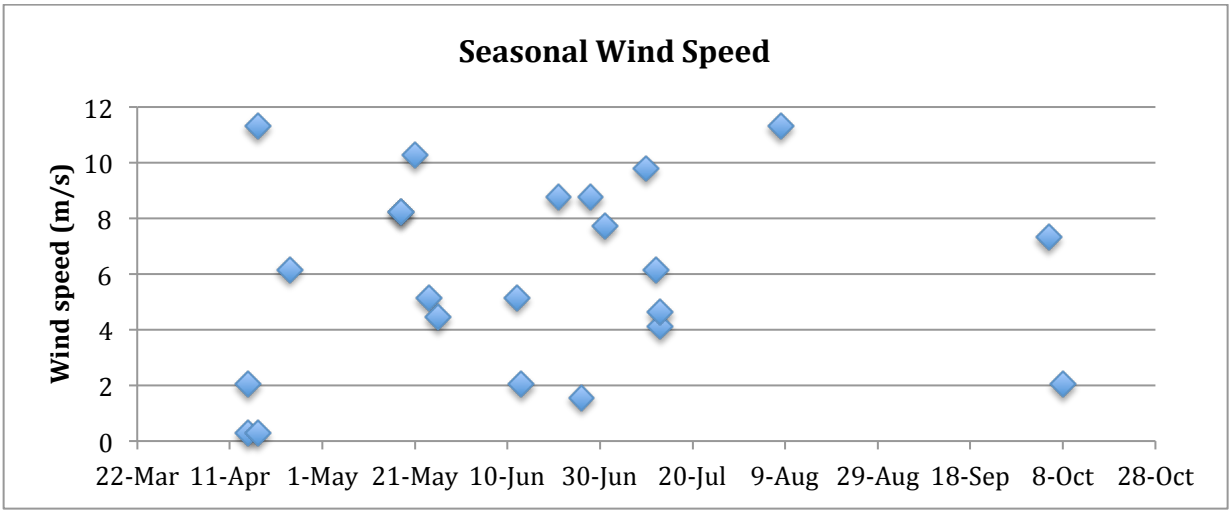

Figure 14. Wind speed shows no significant seasonal dependence, thus the temperature difference between T_s and T_a drives the seasonal cycle in heat flux.

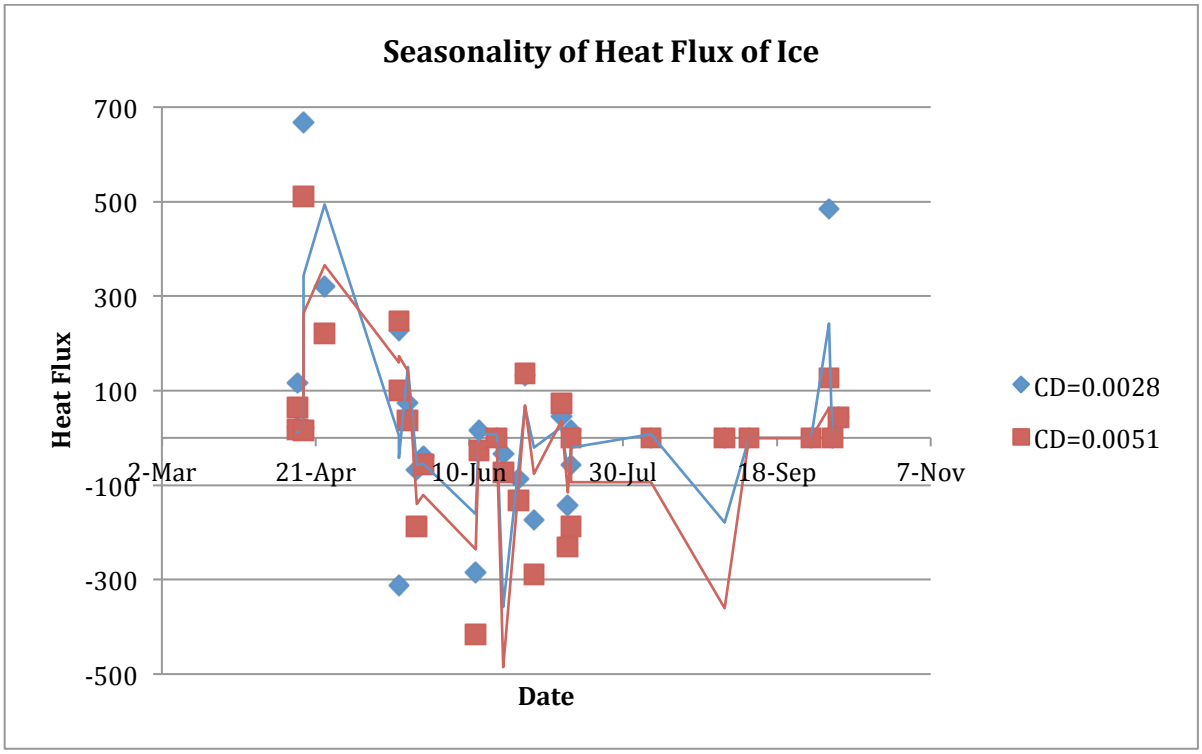

Figure 15. The heat flux of sea ice to air from April to October. The heat flux is positive during onset of melting, negative during the summer months, and positive in October during freeze-up. Data are missing from August and September, as the satellite scene in August was ice-free, and the images from September are of the center of the Arctic where corresponding in-situ air temperature sensors do not measure wind speed. Thus, heat flux could not be calculated for these images.

Surface type matters in heat flux. The air-drag coefficient (C_D) varies for different skin types. C_D for sea ice ranges by a factor of two (0.0019 to 0.0051) depending on ice roughness (Prinsenberg & Peterson, 2002). Ice drift models tend to use 0.0028 as the drag

coefficient, however, it can vary depending on different ice conditions. Figure 15 shows an example of the variation in heat flux for sea ice depending on C_D values of 0.0028 or 0.0051, the two extremes. A smaller C_D would induce a smaller heat flux; a larger C_D would induce a larger heat flux (Figure 15).

Note that ice and water have similar heat flux seasonality, however, the magnitude differs due to a change in variables (Figure 16). Water has a greater range in heat flux than ice, responding to the greater variability in $T_s - T_a$ temperature difference.

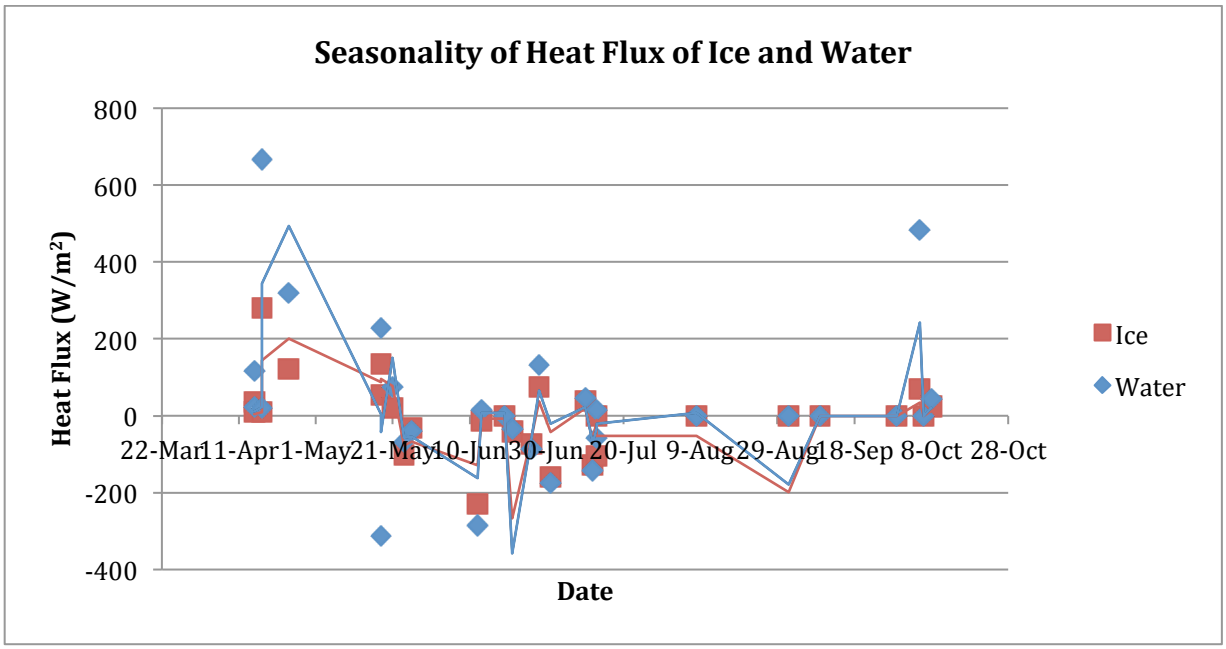

Figure 16. Water and ice share similar seasonality patterns, however, water values range more due to a wider range in temperature differences (T_s - T_a).

Landsat 8 cannot calculate wind speed, and thus in-situ temperature stations are required to measure heat flux in the Arctic. In addition, buoys in the Beaufort Gyre fail to measure wind speed, therefore heat flux measurements in this study are limited to coastal regions where in-situ land temperature stations exist. Note that polar wind speed products are available for MODIS and AVHRR satellites, as well as for SeaWinds on NASA's QuikSCAT satellite. NCEP/NCAR reanalysis wind products are also available (Kalnay et al., 1996). Although these products have a low spatial resolution of 2-4 km, they can be useful in determining wind speed in remote regions of the Arctic in order to measure heat flux.

4. Summary and Discussion

Rapidly changing climate in the Arctic is an important problem with major consequences. The Arctic acts as a cooling blanket to the planet, with its high albedo from sea ice cover. However, as sea ice melts, the planet's albedo will rise, causing increased air and surface temperatures globally. Warmer temperatures will further cause sea ice to melt, causing an ice-albedo feedback, which will continue to raise temperatures. It is important to keep monitoring how temperature and albedo change and respond to one another in the Arctic daily, monthly and annually.

However, land stations are limited and spatially sparse throughout the Arctic's Beaufort Sea region; few territories are consistently measured for temperature. This study hypothesizes that satellite-derived T_s can be used as a tool to approximate T_a in remote regions of the Arctic. Since T_a stays relatively homogeneous over a large area, it can be compared to the satellite-derived T_s of a Landsat 8 satellite image. Studies have measured the difference between T_s and T_a to better understand heat fluxes, or energy exchange between atmosphere-surface boundary layers (Diak & Wipple, 1989; Prigent et al., 2003), as well as have applied satellite-derived T_s to map spatial patterns of T_a in regions of limited T_a data (Vogt et al., 1997). However, no studies have linked T_s – T_a regarding sea ice.

T_s and T_a are fundamentally different in their "meaning, magnitude and measurement technique" (Jin & Dickinson, 2010). T_a is the surface air temperature, or thermodynamic temperature, measured by an in-situ thermometer 3 m above surface. T_s is the skin temperature, or "radiometric surface temperature" (Jin et al., 1997), measured by upwelling longwave radiation from Earth's surface. T_s is measured by inverting the Planck function, using the thermal infrared radiation captured by satellites. T_a is related to T_s, but can vary depending on cloud conditions and land cover (Jin & Dickinson, 2010).

$T_s > T_a$ by 0.56˚C in an average Beaufort region sea ice scene. This difference compared T_a from an in-situ surface air temperature station to the average T_s for the whole scene over the melting season, from April to October. The T_s average showed that T_s and T_a are closely

related, with a correlation of determination of 0.788, however, it does not provide additional information about how T_s and T_a vary by surface type in the Arctic region.

T_a was then compared to T_s of three surface types (ice, melt ponds, water) in each satellite image. These three classes varied greatly throughout the season. Sea ice was covered in snow in April and bare in October; melt ponds were shallow at the onset of melting and deep right before freeze-up. Each surface type was averaged for the whole satellite scene, and then compared to the closest in-situ T_a. The coefficient of determination between T_s and T_a for sea ice was 0.857, 0.852 for melt ponds, and 0.766 for open water. $T_s > T_a$ by 0.11˚C for sea ice and by 1.91˚C for water. Because a majority of the surfaces in the Arctic are sea ice, satellites can therefore act as a tool to estimate T_a.

The difference between T_s and T_a has been measured in mid-latitudes and has given similar results with coefficients of determination of 0.88 and 0.823 (Prigent et al., 2003; Vogt et al., 1997). T_s and T_a vary by 0.5˚C, 2˚C, 2.9˚C, and 3˚C (Kawai & Kawamura, 1997; Vogt et al., 1997; Prigent et al., 2003; Key et al., 1994). $T_s - T_a$ grows in magnitude from tropical to mid-latitudes, increasing from 2.9˚C to 2.95˚C for 40˚N-60˚N (Prigent et al., 2003). Thus, $T_s - T_a$ in the Arctic is expected to have a larger difference. In the Beaufort Sea region, $T_s - T_a$ varies greatly within the same months, however, the mean differences are comparable to mid-latitude studies.

There is strong seasonal variation of $T_s - T_a$. At the beginning of the melting season, $T_s > T_a$ because T_s responds quickly to solar forcings and thus the surfaces warm faster than the surrounding air. In the peak of the melting season, T_a increases with consistent presence of sunlight, and $T_s < T_a$. During the onset of freeze-up in early fall, T_a drops allowing ice to regrow, while T_s stays relatively warmer, causing $T_s > T_a$. All surface types follow the same seasonal cycle of $T_s - T_a$, however, water has the greatest deviation.

Albedo is correlated with T_s and therefore T_a. Lower T_s indicates a higher albedo. Ice, for example, has a low T_s and high albedo, thus reflects incoming radiation. Higher T_s, like water, has a low albedo and therefore absorbs incoming radiation. T_s and albedo have

strong seasonal variation, changing in opposite phases; as temperatures increase during the summer, ice melts and melt ponds deepen, lowering the albedo, and as temperatures decrease in freeze-up, ice re-forms to increase the albedo. Albedo and sea ice thickness are related; lower albedos tend to have thinner ice layers. The Arctic sea ice is getting thinner and thinner, resulting in lower albedo, and increased T_s. As the Arctic undergoes major climate changes, temperatures are expected to increase, causing ice to melt and thus lower surface albedo, causing an ice-albedo feedback.

$T_s - T_a$ is proportional to heat flux. When $T_s > T_a$ in April and May, there is a positive heat flux from the surface to the atmosphere; sea ice warms more quickly than the atmosphere and thus transfers heat to the surrounding air. In the summer, from June to August, $T_s < T_a$, causing a negative heat flux. The air warms and transfers heat back to the sea ice, contributing to further sea ice melting. In October, as freeze-up begins, heat flux is positive, indicating that air temperatures have cooled and sea ice begins to transfer heat back to the atmosphere. This is an important process in the freeze-up months, as this negative heat flux initiates pancake ice formation in the open ocean. Heat flux varies depending on surface type. Heat flux is proportional to a drag coefficient which can vary greatly across different surface types (e.g. vast stretches of open water vs. broken multi-year sea-ice floes, [Guest & Davidson, 1991]). Further, this drag coefficient depends on the sign of $T_s - T_a$, which sets the structure of the atmospheric boundary layer (Garratt, 1994). Future work should consider the dependence of the drag coefficient on surface types and on temperature differences between the air and the surface.

$T_s - T_a$ is a great tool for monitoring heat flux changes in the Arctic, however, wind speed must be known. It is important to note that wind did not have a strong seasonal pattern. However, not all in-situ thermometer stations measure wind speed. Floating IMB and ITP buoys in the center of the Arctic do not have anemometers. Future studies should link sea ice drift patterns with satellite wind speed data products. Sea ice responds differently to wind forcings depending on its composition and thickness (i.e. packed-in ice is less affected by strong winds). However, if sea ice type and composition is known, wind speed can be determined. Please refer to Section 3j for a full discussion.

Global climate models (GCM) must be configured to accurately use T_s and T_a to resolve appropriate surface fluxes and better project future warming in the Arctic. Each GCM has its own method of computing T_s: estimating T_s from T_a, or sometimes using a combination of T_s and T_a. Some GCMs strictly use T_a, while others use T_s. There is no strong definition of T_s and T_a among modelers, leading to inconsistent results. GCM models tend to underestimate T_s, which in turn underestimates the negative longwave flux from the surface to the atmosphere (Prigent et al., 1993). GCMs must better understand the fundamental difference between T_s and T_a to best estimate the changing state of the Arctic.
Landsat 8 is a critical tool for Arctic observation because of its higher spatial resolution than competing scientific satellites, allowing for accurate depictions of each surface type. Sea ice scene surfaces have high heterogeneity, thus surface type must be known. Therefore, Landsat 8 is the preferred satellite. However, Landsat 8 data are currently limited to the Beaufort region and East Greenland. Landsat 8 must add more spatial area to their zones, including more images offshore, to best monitor the changing Arctic climate.

Although Landsat 8 has high spatial resolution, allowing for visual differentiation between surface types, classification techniques are still limited. Sea ice and water are close in proximity, thus surface type varies greatly in a 100 m by 100 m cell capturing TIR. Misclassifications of sea ice and water create errors in satellite-derived T_s, causing ice to be too warm and water to be too cold. Future studies should improve classification techniques to calculate more accurate surface-specific T_s.

The biggest error from calculating T_s using Landsat 8 data is that the emissivity is assumed to be 0.95. This number is the average emissivity of a non-radiating, blackbody surface. A lower emissivity would produce a higher temperature. A sea ice scene with a lower emissivity by 0.05 emissivity leads to a 3˚C increase in temperature (Gordon, 2013). Emissivity of ice is uncertain; Grody et al.'s study (2000) estimates young sea ice to have an emissivity of 0.95 and multiyear ice to have an emissivity of 0.88, while NSIDC (2013b) measured young sea ice at 0.92 and multiyear sea ice at 0.84. In-situ T_s is calculated most accurately by using an infrared radiometer because the land surface emissivity is known (Prigent et al., 2003). Surface emissivity is attainable through SSM/I satellites, however,

those images do not include snow- and ice-free sites. More research must be done to best estimate sea ice surface emissivities in order to most accurately determine T_s of a sea ice scene.

Both in-situ air temperature and satellite data are limited in the Arctic. Land stations are spatially sparse, and satellite data can only be interpreted in well-lit months and cloud-free days. T_s and T_a comparisons in the Arctic requires more data for future work.

Acknowledgements
I kindly acknowledge the guidance from my advisor, Professor Mary-Louise Timmermans, for overseeing and critiquing the study; this work would not have been possible without her support. Thank you to Larry Bonneau, the heart behind the Yale Center for Earth Observation, for remote sensing consultations and encouragement. A final thank you to Professor Ron Smith for his support at the beginning of the process.

References

Allison, I., Brandt, R. E., & Warren, S. G. (1993). East Antarctic sea ice: Albedo, thickness distribution, and snow cover. *Journal of Geophysical Research: Oceans (*

1978–2012), *98*(C7), 12417-12429.

Björk, G., Stranne, C., & Borenäs, K. (2013). The Sensitivity of the Arctic Ocean Sea Ice Thickness and Its Dependence on the Surface Albedo Parameterization. *Journal of Climate*, *26*(4).

Casey, K. S., & Cornillon, P. (1999). A comparison of satellite and in situ-based sea surface temperature climatologies. *Journal of Climate*, *12*(6).

Diak, G. R., & Whipple, M. S. (1995). Note on estimating surface sensible heat fluxes using surface temperatures measured from a geostationary satellite during FIFE 1989. *Journal of Geophysical Research: Atmospheres (1984–2012)*, *100*(D12), 25453-25461.

Garratt, J. R. (1994). *The atmospheric boundary layer*. Cambridge university press.

Gordon, A. (2013). *Seasonal Arctic Sea Ice: The perfect recipe for a runaway ice-albedo feedback.* Unpublished paper. Department of Geology and Geophysics, Yale University, New Haven, CT.

Grenfell, T. C., & Perovich, D. K. (1984). Spectral albedos of sea ice and incident solar irradiance in the southern Beaufort Sea. *Journal of Geophysical Research: Oceans (1978–2012)*, *89*(C3), 3573-3580.

Grody, N., F. Weng, R. Ferraro, Application of AMSU for obtaining hydrological parameters, *Microwave Radiometry and Remote Sensing of the Earth's Surface and Atmosphere*P. Pampaloni, S. Paloscia, 339–351, VSP, Zeist, Netherlands, 2000.

Guest, P. S., & Davidson, K. L. (1991). The aerodynamic roughness of different types of sea ice. *Journal of Geophysical Research: Oceans (1978–2012)*, *96*(C3), 4709-4721.

Jin, M., Dickinson, R. E., & Vogelmann, A. M. (1997). A comparison of CCM2/BATS skin temperature and surface-air temperature with satellite and surface observations *J. Clim.* **10** 1505-24

Jin, M., & Dickinson, R. E. (2002). New observational evidence for global warming from satellite. *Geophysical research letters*, *29*(10), 39-1.

Jin, M., & Dickinson, R. E. (2010). Land surface skin temperature climatology: benefitting from the strengths of satellite observations. *Environmental Research Letters*, *5*(4), 044004.

Kalnay, E., Kanamitsu, M., Kistler, R., Collins, W., Deaven, D., Gandin, L., ... & Joseph, D. (1996). The NCEP/NCAR 40-year reanalysis project. *Bulletin of the American meteorological Society*, *77*(3), 437-471.

Kawai, Y., & Kawamura, H. (1997). Characteristics of the satellite-derived sea surface temperature in the oceans around Japan. *Oceanographic Literature Review*, *44*(11), 1383-1383.

Key, J., Maslanik, J. A., Papakyriakou, T., Serreze, M. C., & Schweiger, A. J. (1994). On the validation of satellite-derived sea ice surface temperature. *Arctic*, *47*(3), 280-287.

Køltzow, M, (2003). Observations of sea ice albedo. Norweigan Meteorological Institute.

Kwok, R., & Untersteiner, N. (2011). The thinning of Arctic sea ice. *Phys. Today*, *64*(4), 36-41.

Liang, S. (2005). *Quantitative remote sensing of land surfaces* (Vol. 23). Wiley-Interscience, 324-325.

Lindsay, R. W. (2001). Arctic sea-ice albedo derived from RGPS-based ice-thickness estimates. *Annals of Glaciology*, *33*(1), 225-229.

National Snow & Ice Data center (2013). Environment: Trends. In *All About Sea Ice.* Retrieved April, 2013, from <http://nsidc.org/cryosphere/seaice/environment/trends.html>.

NSIDC (2013b), Calculating Sea Ice Concentration from ESMR. Retrieved March, 2014, from <https://nsidc.org/data/docs/daac/nsidc0009_esmr_seaice/arctic_ice_concentration.html>.

Overland, J. E., K. R. Wood and M. Wang, 2011: Warm Arctic-cold continents: Impacts of the newly open Arctic Sea. *Polar Res.*, 30, 15787, doi: 10.3402/polar.v30i0.15787.

Perovich, D. K., Grenfell, T. C., Light, B., & Hobbs, P. V. (2002). Seasonal evolution of the albedo of multiyear Arctic sea ice. *Journal of Geophysical Research: Oceans (1978–2012)*, *107*(C10), SHE-20.

Perovich, D. K., & Richter-Menge, J. A. (2009). Loss of sea ice in the arctic*. *Annual Review of Marine Science*, *1*, 417-441.

Perovich, D., J. Richter-Menge, B. Elder, T. Arbetter, K. Claffey, and C. Polashenski (2013). Observing and understanding climate change: Monitoring the mass balance, motion, and thickness of Arctic sea ice, http://IMB.crrel.usace.army.mil

Prigent, C., Aires, F., & Rossow, W. B. (2003). Land surface skin temperatures from a combined analysis of microwave and infrared satellite observations for an all-weather evaluation of the differences between air and skin temperatures. *Journal of Geophysical Research: Atmospheres (1984–2012)*, *108*(D10).

Prinsenberg, S., & Peterson, I. K. (2002). Variations in air-ice drag coefficient due to ice surface roughness. *International Journal of Offshore and Polar Engineering*, *12*(2), 121-125.

Tou, J. T. and R. C. Gonzalez, 1974. *Pattern Recognition Principles*, Addison-Wesley Publishing Company, Reading, Massachusetts.

Tschudi, M. A., Curry, J. A., & Maslanik, J. A. (2001). Airborne observations of summertime surface features and their effect on surface albedo during FIRE/SHEBA. *Journal of Geophysical Research: Atmospheres (1984–2012)*, *106*(D14), 15335-15344.

USGS (2013). DOI/GTN-P Climate and Active-Layer Data Acquired in the National Petroleum Reserve–Alaska and the Arctic National Wildlife Refuge, 1998–2011. Retrieved from, <http://pubs.usgs.gov/ds/812/CamdenBay/CamdenBay.html>

USGS (2014). Calibration Notices. Retrieved from <http://landsat.usgs.gov/calibration_notices.php>

Vogt, J. V., Viau, A. A., & Paquet, F. (1997). Mapping regional air temperature fields using satellite-derived surface skin temperatures. *International Journal of Climatology*, *17*(14), 1559-1579.

Appendix

For full details of Appendix material, please refer to previous report (Gordon, 2013).

Masking

To define the study area, the region of interest tool was used. Data along the edges of the original images are sometimes poorly calibrated, so the outside edges must be masked out. The ROI was exported as a vector because a vector file can be applied to any region, with any band. Thus, both images could share the same ROI, rather than re-creating a new region for each image separately. This vector was then loaded into ENVI.

Next, a mask was built. The mask was built to fit the calibrated Landsat 8 images by selecting the vector file. Then, the mask was applied to the calibrated image. The spatial subset was selected to ROI/EVF as the study area vector to create the bounding box. The total sample was 4673, and the total lines were 3748. These numbers are crucial to remember, as each image might have an extra column or row, and they should all be the same with the new mask. The mask value was set as NaN so that the pixels outside of the bounding box had no value, instead of 0.

In addition to the study region, all clouds (cirrus and low-lying clouds) were masked out. A mask can be made of just the cirrus clouds by opening the cirrus band, creating ROIs, converting to a vector file, and then building a mask. Low-lying clouds, such as cumulus and stratus clouds, can be masked out by loading a 732-RGB of the multispectral image; ice

appears blue, while clouds appear pink, so they can easily be identified to create ROIs and mask them out.

These same steps used to create a study region and mask clouds, were applied to all images. The masked image allows for calculating statistics of albedo and T_s, for example, without including numbers from areas outside the study region or from clouds. Cirrus clouds, in particular, tend to produce lower temperatures than in-situ measurements, since the satellite measures the cloud-top temperature, rather than the T_s. Therefore, with temperature measurements, it is extremely important to mask out all clouds.

Unsupervised Classification

Once the study area is defined, the scene can be separated into classes to further process information. Four classes were created statistically using K-Means unsupervised classification: ice and water, and two classes representing a different mixture of ice and water, using the masked calibrated Landsat 8 images. The spectral signature of the classes clearly marked the reflectance differences.

Images with land were separated into five classes: land, ice water, and two mixed ice/water pixels. To find averages of classes, the land was masked to ensure only the ice and water temperatures and albedos were from the sea, versus including the land measurements. The only land temperatures measured were in places where a land-surface T_a base was located, such as Barrow, Point Hope, and Sachs Harbour, to compare skin temperature and in-situ air temperature at the exact same coordinates. Otherwise, temperatures and albedos from land regions were omitted.

K-Means randomly finds the initial cluster centroid, and assigns surrounding pixels to a centroid using the minimum Euclidean distance principle. K-Means was selected to statistically cluster four classes: ice and water, and two classes representing a different mixture of ice and water, using the masked calibrated Landsat 8 images. A change threshold of 5%, and 10 maximum iterations were selected. The spectral signature of the classes clearly marked the reflectance differences.

The K-Means classification was tested for accuracy against a separate unsupervised classification from ISODATA. A change threshold of 5% and 10 maximum iterations were selected; the number of possible classes ranged from 2 to 7.

Computing Albedo

To calculate the albedo, a Landsat image must first be calibrated from digital numbers to Top of Atmosphere (TOA) reflectance. This calibrated image uses the six Landsat bands and each pixel is represented by a reflectance value ranging from 0 to 1, stored in a floating point data format.

Albedo can be calculated with various algorithms from satellite sensors. Because albedo is measured as the average reflectance of the sun's spectrum, all wavelengths are considered and weighted differently. Two separate algorithms were previously tested and the algorithm developed by Liang (2000) and normalized by Smith (2010) was deemed most accurate and will thus be used in this report (Gordon, 2013).

The Landsat shortwave albedo calculation is as follows:

$\rho = (0.356\ \rho 2 + 0.130\ \rho_4 + 0.373\ \rho_5 + 0.085\ \rho_6 + 0.072\ \rho_7 - 0.0018)/\ 1.016$

where ρ represents Landsat bands 2, 4, 5, 6 and 7 (blue, red, near-IR, and mid-IR bands).

Computing Skin Temperature

In order to calculate T_s the Landsat image must be reprocessed to a radiance value. The newly calibrated image uses one Landsat thermal band, and each pixel is represented by a radiance value, stored as a floating point, instead of as a digital number. To convert radiance to temperature in kelvin, without atmospheric correction, uses the following math:

$$T = \frac{K_2}{\ln\left(\frac{K_1 * \varepsilon}{CV_{R1}} + 1\right)}$$

where T is degrees in Kelvin, CV_{R1} is the cell value in radiance, and ε is the emissivity. The typical emissivity of an object is 0.95, so that number is used.

In ENVI, the formula looks slightly different: k2 / alog (((k1 *0.95)/B1)+1) where band 1 is matched with the radiance band created during the recalibration, and emissivity is 0.95. K2 and K1 values are given by the temperature band metadata.